Comparison of approximations in density functional theory calculations: Energetics and structure of binary oxides

Yoyo Hinuma, Hiroyuki Hayashi, Yu Kumagai, Isao Tanaka, and Fumiyasu Oba

Phys. Rev. B **96**, 094102 — Published 5 September 2017

DOI: 10.1103/PhysRevB.96.094102

Comparison of approximations in density functional theory calculations: Energetics and structure of binary oxides

Yoyo Hinuma [1,2,3]*, Hiroyuki Hayashi [1], Yu Kumagai [4,5], Isao Tanaka [1,2,6,7] and Fumiyasu Oba [8,4,2]**

[1] Department of Materials Science and Engineering, Kyoto University, Kyoto 606-8501, Japan
[2] Center for Materials Research by Information Integration, Research and Services Division of Materials Data and Integrated System, National Institute for Materials Science, Tsukuba 305-0047, Japan
[3] Center for Frontier Science, Chiba University, Chiba 263-8522, Japan
[4] Materials Research Center for Element Strategy, Tokyo Institute of Technology, Yokohama 226-8503, Japan
[5] PRESTO, Japan Science and Technology Agency, Kawaguchi 332-0012, Japan
[6] Elements Strategy Initiative for Structural Materials, Kyoto University, Kyoto 606-8501, Japan
[7] Nanostructures Research Laboratory, Japan Fine Ceramics Center, Nagoya 456-8587, Japan
[8] Laboratory for Materials and Structures, Institute of Innovative Research, Tokyo Institute of Technology, Yokohama 226-8503, Japan

* yoyo.hinuma@gmail.com
** oba@msl.titech.ac.jp

ABSTRACT

High-throughput first-principles calculations based on density functional theory (DFT) is a powerful tool in data-oriented materials research. The choice of approximation to the exchange-correlation functional is crucial as it strongly affects the accuracy of DFT calculations. This study compares performance of seven approximations based on Perdew-Burke-Ernzerhof (PBE) generalized gradient approximation (GGA) with and without Hubbard *U* and van der Waals corrections, which are PBE, PBE+*U,* PBED3, PBED3+*U,* PBEsol, and PBEsol+*U*, and the strongly constrained and appropriately normed (SCAN) meta-GGA on the energetics and crystal structure of elementary substances and binary oxides. For the latter, only those with closed-shell electronic structures are considered, examples of which include Cu_2O, Ag_2O, MgO, ZnO, CdO, SnO, PbO, Al_2O_3, Ga_2O_3, In_2O_3, La_2O_3, Bi_2O_3, SiO_2, SnO_2, PbO_2, TiO_2, ZrO_2, HfO_2, V_2O_5, Nb_2O_5, Ta_2O_5, MoO_3, and WO_3. Prototype crystal structures are selected from the Inorganic Crystal Structure Database (ICSD), and cation substitution is used to make a set of existing and hypothetical oxides. Two indices are proposed to quantify the extent of lattice and internal coordinate relaxation during a calculation. The former is based on the second invariant and determinant of the transformation matrix of basis vectors from before relaxation to after relaxation, and the latter is derived from shifts of internal coordinates of atoms in the unit cell. PBED3, PBEsol, and SCAN reproduce experimental lattice parameters of elementary substances and oxides well with few outliers. Notably, PBEsol and SCAN predict the lattice parameters of low dimensional structures comparably well with PBED3, even though these functionals do not explicitly treat van der Waals interactions. SCAN gives formation enthalpies and Gibbs free energies closest to experimental data, with mean errors (MEs) of 0.01 and -0.04 eV, respectively, and root-mean-square errors (RMSEs) are both 0.07 eV. In contrast, all GGAs including those with Hubbard *U* and van der Waals corrections give 0.1 to 0.2 eV MEs and at least 0.11 eV RMSEs. Phonon contributions of solid phases to the formation enthalpies and Gibbs free energies are estimated to be small at less than ~0.1 eV/atom within the quasiharmonic approximation. The same crystal structure appears as the lowest energy polymorph with different approximations in most of the investigated binary oxides. However, there are some

systems where the choice of approximation significantly affects energy differences between polymorphs, or even the order of stability between phases. SCAN is the most reasonable regarding relative energies between polymorphs. The calculated transition pressure between polymorphs of ZnO and SnO_2 is closest to experimental values when PBED3, PBEsol (also PBED3+*U* and PBEsol+*U* for ZnO), and SCAN are employed. In summary, SCAN appears to be the best choice among the seven approximations based on the analysis of the energetics and crystal structure of binary oxides, while PBEsol is the best among the GGAs considered and shows a comparably good performance with SCAN for many cases. The use of PBEsol+*U* alongside PBEsol is also a reasonable choice, given that *U* corrections are required for several materials to qualitatively reproduce their electronic structures.

I. INTRODUCTION

Metal oxides are an important class of materials because of its abundance and diversity of functionalities. Their applications include, but not limited to, capacitors, thermistors, varistors, magnets, electronic devices, phosphors, catalysts, and photocatalysts [1-10]. A fair amount of experimental and theoretical research has been conducted on metal oxides from both fundamental and technological points of view. As a result, crystal structures and fundamental properties are now known for many oxides. For instance, there are more than 70,000 entries of metal oxides in the Inorganic Crystal Structure Database (ICSD), where there are 40,000 distinct oxides with different stoichiometries and space groups [11].

Data-oriented approaches are rapidly growing in recent years and have been applied to materials research. In particular, high-throughput first-principles calculations based on density functional theory (DFT) [12,13] are powerful when generating large data for both known and hypothetical materials [14-18]. With the aid of methods for high-throughput computations [17,19-25], such data have been used in many studies for understanding the tendency of physical and chemical properties and exploring novel materials [26-43], some of which effectively combine machine learning techniques [33-36]. High-throughput first-principles calculations have also been used for studying

metal oxide systems, for instance to explore transparent conducting oxides [37,38], photocatalysts [39-41], and high-κ dielectrics [42].

DFT in conjunction with the Kohn-Sham scheme [12,13] fundamentally allows us to quantify the total energies of many-electron systems from the charge density only. However, since the exact functional form is not known, the choice of approximation to the exchange correlation remains an important issue [44]. The local density approximation (LDA) [13] and the generalized gradient approximation (GGA) [45] are commonly used approximations. It is known that functionals within the LDA and GGA cannot give accurate total energies simultaneously for diverse systems with different crystal and electronic structures, and tend to underestimate and overestimate the lattice constants, respectively. These shortcomings affect the physical quantities such as the band structure, vibrational frequencies, ionization potential, defect formation properties, and so forth. Therefore, many variants of the GGA and beyond, such as meta-GGAs [44,46-48], and those with additional correction terms for describing on-site Coulomb [49,50] and van der Waals interactions [51-54] have been designed so far to improve the accuracy.

Approximations that include non-local exchange, such as hybrid functionals [55-59] and the screened exchange [60], have been reported to perform better in the prediction of structural and electronic properties for a variety of semiconductors and insulators [61-67]. In addition, approaches based on many-body perturbation theory, as well as explicit many-body calculations, can yield even more accurate results [68-71]. However, such calculations are computationally demanding and so ill-suited for high-throughput studies. In addition, one-electron states from the LDA and GGA often serve as inputs in not only these many-body methods but also non-self-consistent hybrid functional approaches for accelerating calculations [72,73]. There exist a number of recent studies comparing the performance of various GGA and meta-GGA functionals [74-77], but we are not aware of a study that systematically investigates the differences in relative energy between polymorphs of the same stoichiometry.

In this article we investigate how the use of different approximations to the exchange-correlation functional affects the lattice parameters of elementary substances and binary oxides as well as the relative energy between different polymorphs of binary

oxides. We focus on binary oxides with formally closed-shell electronic structures. Although studies including systems with partially occupied *d* states are unarguably important, they are in a different class of materials from the viewpoint of electronic and magnetic structure, and are very likely to require different treatment compared to the closed-shell systems. We consider the Perdew-Burke-Ernzerhof (PBE) functional [78], which is currently the most popular GGA functional, and the PBEsol functional [79] that is a modification of the PBE functional tuned for solids. For low dimensional (LD) semiconductors and/or insulators, it is well known that the van der Waals interactions play a crucial role for predicting the lattice parameters, for instance, interlayer distances in layered structures. Recently, Grimme *et al*. designed a procedure to make dispersion corrections to standard DFT functionals (DFT-D3), which is based only on relative atomic positions, and tested their approach on interactions between molecules and/or complexes [53]. We therefore consider their D3 correction to PBE (PBED3) and evaluate its performance on periodic oxide crystals. In addition, these GGA functionals with Hubbard *U* correction [49,50], which are denoted as PBE+*U*, PBED3+*U*, and PBEsol+*U*, are employed to improve the description of localized *d* and *f* states. The need for such corrections has been reported for not only partially filled states but also formally filled and empty states [49,50,80-83]. The performance of the recently proposed strongly constrained and appropriately normed (SCAN) meta-GGA [48] is also investigated. Differences in crystal structure, formation energy, and phase transition pressure between theory and experiment are discussed, together with a procedure to quantitatively express the amount of lattice and internal coordinate deformation.

II. METHODOLOGY

A. First-principles calculations

First-principles calculations were conducted using the projector augmented-wave method [84] and the approximations to the exchange-correlation interactions including PBE [78], PBED3 [53], and PBEsol [79], and the SCAN meta-GGA [48] as implemented in the VASP code [85,86]. The effect of adding the Hubbard *U* was additionally considered on the basis of Dudarev's formulation [50]. The effective *U* value, *U*-*J* , which is hereafter denoted as U_{eff}, was set at 3 eV for the

valence *d* states of Ti, V, Cr, Mn, Zr, Nb, Mo, Tc, Ru, Rh, Pd, La, Hf, Ta, W, Re, Os, Ir, Pt and Au, and 5 eV for the valence *d* states of Fe, Co, Ni, Cu, Zn, Ga, and Ag. In addition, U_{eff} of 5 eV was applied on the 4*f* states of Ce. These U_{eff} values are mostly the same as those used to obtain fitted elemental-phase reference energies (FERE) by Stevanović *et al.* [87]; U_{eff} for Fe, Co, and Ni were changed to 5 eV as self-consistent U_{eff} derivations give U_{eff} values closer to 5 eV rather than 3 eV [88,89]. The +*U* corrections were applied to oxides of group 4, 5, and 6 elements with d^0 formal electronic configurations because the corrections would be necessary when treating their defects, where electrons locally enter the *d* orbitals, or when comparing results with metal oxides having other oxidation states. Non-zero U_{eff} values were also employed for Zn and Ga because correction to the semicore *d*-states may become necessary to avoid excessive hybridization with oxygen 2*p* orbitals [81].

Seven kinds of approximations in total, which are PBE, PBE+*U*, PBED3, PBED3+*U*, PBEsol, PBEsol+*U*, and SCAN, are considered in the present study. When comparing results with and without +*U* over a same set of systems, we may include results with U_{eff}=0, *i.e.* those without +*U*, in the set of +*U* results. This treatment is necessary, for instance, to compare means of differences between calculated and experimental formation enthalpy over the same set of systems. In such cases, the approximation is denoted using (+*U*) in brackets, for example as PBE(+*U*). A plane wave basis set with an energy cutoff of 550 eV was used. Even *k*-point meshes were used in geometry optimization, which were determined on the basis of the convergence of total energies: the criterion of the total energy change was set at 0.005 meV per atom per the number of incremental *k* points.

Experimentally reported structures of binary oxides investigated in this study were taken from the ICSD [11], and those listed in Table I were used as "prototypes", which are each a representative of a given crystal structure. The cation of the prototype was substituted with an isovalent cation shown in Table II to form a set of known and hypothetical oxide structures. However, not all crystal structures reported in the ICSD were selected as prototypes. Structures containing sites with partial occupancies were not considered. Other reasons for not considering include no establishment of the crystal structure (example: low temperature tridymite), excessively large unit cells (example:

ICSD coll code 86279, $Si_{96}O_{192}$ in the Zeolite-ZSM-5-frame structure type; the largest primitive cell in this study contains 40 atoms), and no existence of compounds that are computationally metastable by less than 0.2 eV/atom in all approximations (example: ICSD coll code 51176, Nb_2O_5 in the Nb_2O_5 (HP) structure type). Lattice parameters and internal coordinates were relaxed such that stresses and atomic forces are less than 0.2 GPa and 0.01 eV/Å (0.001 GPa and 0.0003 eV/Å for LD structures as defined in Section IIIA). No symmetry breaking was allowed during relaxation, but relaxation to a supergroup of the original space group type is possible via geometry optimization.

The formation enthalpy and Gibbs free energy were assessed via phonon calculations and thermodynamic function evaluation within the quasiharmonic approximation. The finite displacement approach as implemented in the Phonopy code [90] was used with the PBEsol functional and the VASP code. The pressure was set to 0 GPa in the calculations. The Gibbs free energy (G) at 298 K and 0 GPa was evaluated via minimization of the Helmholtz free energy with respect to the volume. The enthalpy (H) was obtained by adding temperature times entropy to the Gibbs free energy. Experimental data at 298.15 K and 0.1 GPa was employed instead of calculated values for the O_2 gas phase when obtaining the formation enthalpy and Gibbs free energies of oxides: zero point energy E_{ZPE} = 0.05 eV/atom, H-E_0 = 0.09 eV/atom, and G-E_0 = -0.27 eV/atom [91], where E_0 is the total energy excluding vibrational contributions at 0 K.

B. Detection of significant relaxation

Significant spontaneous relaxation can happen during a calculation, especially when the initial structure is highly unstable. Large changes in the crystal structure can happen on the lattice, internal coordinates, or both.

Figure 1 shows relaxation of Li_2O in the rhombohedral 102 Anti-$CdCl_2$(3R) prototype with PBE. There is not much change in internal coordinates, but the c/a ratio of the conventional cell decreases significantly from 4.46 to 2.50. The resulting structure is the 103 Anti-Fluorite-CaF_2 prototype; $\mathbf{a}_{102}$, $\mathbf{b}_{102}$, and $\mathbf{c}_{102}$ basis vectors of the conventional cell of the 102 Anti-$CdCl_2$(3R) prototype are related to the $\mathbf{a}_{103}$,

$\mathbf{b}_{103}$, and $\mathbf{c}_{103}$ basis vectors of the conventional cell of the 103 Anti-Fluorite-CaF_2 prototype by

$$\left(\mathbf{a}_{102},\mathbf{b}_{102},\mathbf{c}_{102}\right)=\frac{1}{2}\left(\mathbf{a}_{103},\mathbf{b}_{103},\mathbf{c}_{103}\right)\begin{pmatrix}1 & \bar{1} & 2\\ 0 & 1 & 2\\ \bar{1} & 0 & 2\end{pmatrix}.$$

On the other hand, Fig. 2 shows relaxation of CaO in the hexagonal 206 HgS prototype with PBE. The change of *c*/*a* ratio is very small from 2.42 to 2.45, but the internal coordinates undergo a large change. The coordination of atoms increases from two-fold to six-fold and cations and anions position on top on each other along the *c*-axis upon relaxation. The final structure is the 201 NaCl prototype, where the $\mathbf{a}_{206}$, $\mathbf{b}_{206}$, and $\mathbf{c}_{206}$ basis vectors of the conventional cell of the 206 HgS prototype is related to the $\mathbf{a}_{201}$, $\mathbf{b}_{201}$, and $\mathbf{c}_{201}$ basis vectors of the conventional cell of the 201 NaCl prototype by

$$\left(\mathbf{a}_{206},\mathbf{b}_{206},\mathbf{c}_{206}\right)=\frac{1}{2}\left(\mathbf{a}_{201},\mathbf{b}_{201},\mathbf{c}_{201}\right)\begin{pmatrix}1 & \bar{1} & 2\\ 0 & 1 & 2\\ \bar{1} & 0 & 2\end{pmatrix}.$$

In another example, Fig. 3 shows relaxation of hexagonal 303 Al_2O_3 in the 303 La_2O_3 prototype with PBE. The *c*/*a* ratio changes from 1.56 to 2.54 and there is a large change in internal coordinates as a gap appears between Al_2O_3 layers.

Based on the above observations, there is a serious need to decide whether the crystal structure after relaxation can be judged to still belong to the original prototype. In particular, it does not make sense to call a structure with the original prototype name when the structure has relaxed to a different prototype. This issue raises the problem of designing a robust and automatic procedure without relying on visual inspection to quantitatively describe the extent of relaxation. Hydrostatic, or isotropic, expansion and contraction of the unit cell is not considered as a concern because substituting atoms will naturally change the bond length and change the cell volume. However, excessive deviatoric deformation, such as large *c*/*a* ratio change in hexagonal or tetragonal crystal

families, and/or significant change in internal coordinates must be regarded as a deviation from the original prototype.

We hereby propose a method that quantitatively indicates the extent of relaxation using a limited number of indices. In essence, the deviatoric deformation of the lattice is evaluated based on invariants of the transformation matrix linking lattice vectors before and after relaxation, and the average displacement of internal coordinates is used to evaluate relaxation of atoms within the lattice.

The basis vectors of the primitive cell before and after relaxation are defined as $(\mathbf{a},\mathbf{b},\mathbf{c})$ and $(\mathbf{a}',\mathbf{b}',\mathbf{c}')$, respectively, and are not retaken during relaxation. In other words, after an infinitesimal relaxation of the lattice, the basis vectors infinitesimally change without a discrete jump. We define the transformation matrix $\boldsymbol{M}$ as $(\mathbf{a}',\mathbf{b}',\mathbf{c}')=(\mathbf{a},\mathbf{b},\mathbf{c})\boldsymbol{M}$, which can be written as and separated into two parts as $\boldsymbol{M}=\{\det(\boldsymbol{M})\}^{1/3}\boldsymbol{M}'$, where $\boldsymbol{M}'$ can be interpreted as a volume-conserving transformation. If a supercell related by the matrix $\boldsymbol{P}$ to $(\mathbf{a},\mathbf{b},\mathbf{c})$ and $(\mathbf{a}',\mathbf{b}',\mathbf{c}')$ are used, or in other words, if $(\mathbf{a},\mathbf{b},\mathbf{c})\boldsymbol{P}$ and $(\mathbf{a}',\mathbf{b}',\mathbf{c}')\boldsymbol{P}$ are used instead of $(\mathbf{a},\mathbf{b},\mathbf{c})$ and $(\mathbf{a}',\mathbf{b}',\mathbf{c}')$, then we find $(\mathbf{a}',\mathbf{b}',\mathbf{c}')\boldsymbol{P}=(\mathbf{a},\mathbf{b},\mathbf{c})\boldsymbol{PM}$ or $(\mathbf{a}',\mathbf{b}',\mathbf{c}')=(\mathbf{a},\mathbf{b},\mathbf{c})\boldsymbol{PMP}^{-1}=\{\det(\boldsymbol{M})\}^{1/3}(\mathbf{a},\mathbf{b},\mathbf{c})\boldsymbol{PM'P}^{-1}$. Three quantities related to $\boldsymbol{M}'$ and $\boldsymbol{PM'P}^{-1}$, which are the invariants of $\boldsymbol{M}$, are the same for any $\boldsymbol{P}$. These three values are used to express the extent of deformation of the lattice. The first and third order invariants are the trace and determinant of $\boldsymbol{M}'$, respectively, and the determinant is unity by definition. The second order determinant is most interesting. The von Mises criterion, also known as the maximum distortion strain energy criterion, uses the second-order invariant of the deviatoric stress tensor σ'_{ij} and states that a material would fail if the von Mises stress, $\sqrt{(3/2)\sigma'_{ij}\sigma'_{ji}}$, exceeds the yield stress. In a similar spirit, we use an index based on the second order invariant of $\boldsymbol{M}'$,

$$LR_2 = \boldsymbol{M}'_{ij}\boldsymbol{M}'_{ji} - 3,$$

as a measure of lattice deformation. LR_2 becomes 0 when there is no change in the lattice vectors, which is also the case in transformation of cubic lattices without symmetry breaking because $\boldsymbol{M}'$ is the identity matrix by virtue of symmetry. A large LR_2 represents a large deviatoric deformation of the lattice. One can also use indices based on the trace, $LR_1 = tr(\boldsymbol{M}') - 3 = \boldsymbol{M}'_{ii} - 3$, or the determinant of $\boldsymbol{M}$, $LR_3 = \det(\boldsymbol{M}) - 1$, which are both defined to be zero in case of no transformation. However, LR_1 could not appropriately capture the change in interaxial angles as only the diagonal elements of $\boldsymbol{M}'$ are sampled, whereas LR_2 depends on all nine elements. LR_3 is useful when there is interest in volume change of the unit cell, but is irrelevant in the current study.

No collective drift of atoms is assumed when discussing the relaxation of internal coordinates. This requirement is typically imposed in most calculation schemes as otherwise the average force on atoms would be never non-zero and atoms would continue to collectively drift along a certain direction. Comparison of displacement of internal coordinates in Cartesian coordinates before and after change in lattice vectors is meaningless. Denoting the fractional coordinates of atom i before relaxation as $(x_i, y_i, z_i)^{\mathrm{T}}$ and after relaxation as $(x'_i, y'_i, z'_i)^{\mathrm{T}}$, we define the coordinate relaxation index as

$$CR = \sqrt{\sum_i \left| (\mathbf{a}', \mathbf{b}', \mathbf{c}')(x'_i - x_i, y'_i - y_i, z'_i - z_i)^{\mathrm{T}} \right|^2} \Big/ \sum_i 1.$$

In words, we convert displacements in fractional coordinates to actual distances in Cartesian coordinates using the relaxed basis vectors, and then we find the root mean square of the displacements. CR becomes 0 when there are no degrees of freedom in

internal coordinates and there is no symmetry breaking in the interactions. The dimension of CR in this definition is length, but can be normalized using the average volume per atom and made dimensionless as

$$CR' = \frac{\sqrt{\sum_i \left| (\mathbf{a}', \mathbf{b}', \mathbf{c}')(x_i' - x_i, y_i' - y_i, z_i' - z_i)^{\mathrm{T}} \right|^2}}{\sqrt[3]{\det(\mathbf{a}', \mathbf{b}', \mathbf{c}')} \sum_i 1},$$

where the sum of *i* is over all atoms in a unit cell. We stress that the change in internal coordinates must be referred to the relaxed lattice, not the original lattice. Taking the original lattice as the reference is attractive when discussing the difference between experimental and computed structures of the same crystal, but is not suitable when comparing results of crystals with different constituent elements. Assume we have experimental information on bixbyite (C-type rare earth) structure La_2O_3 with lattice parameter 11.4 Å, and use this as an initial structure to investigate the as-yet-unreported bixbyite structure Al_2O_3. The calculated lattice parameter is about 8.9 Å, which has more than 20% difference from La_2O_3. The relaxation in internal coordinates of Al_2O_3 from those in La_2O_3 should definitely be scaled to the lattice parameter of Al_2O_3.

A "significant relaxation" in this study is defined as a relaxation exceeding at least one of $LR_2 > 0.2$ and $CR > 0.25$Å, where the original prototype is regarded as the crystal structure before relaxation. It is impossible to provide a universally valid threshold, but these values appear to be reasonable in the scope of our work. We do not blindly consider that the original prototype is the "correct" crystal and a large LR_2 or CR in one approximation over another is a failure of an approximation. The same crystal structure (lattice parameters and internal coordinates) is used as the initial structure for a given prototype regardless of the cation species. Non-zero LR_2 is expected for non-cubic lattices and non-zero CR if there is at least one unfixed internal coordinate. We simply want to detect and remove structures that underwent excessive relaxation because we are interested in discussing the lattice parameters and formation energy for a given prototype. Significant relaxation cases, including 102 anti-$CdCl_2$(3R) prototype to 103 anti-Fluorite-CaF_2 prototype in Li_2O, Na_2O, and K_2O, and from 205 HgO, 206 HgS, 207 Massicot prototypes to 201 NaCl prototype in MgO, CaO, SrO, BaO, and CdO, to name

a few, were successfully identified and removed from further analysis.

III. Results and discussion

A. Lattice parameters

The errors in lattice parameters between calculations and experiments are investigated. Computational lattice parameters are evaluated at 0 K. The experimental lattice parameters are obtained from the ICSD according to the following preference criteria: (1) high pressure data are avoided (>1 MPa) and data with pressure information close to 0.1 MPa are preferred over data with no information, (2) high temperature data are avoided (>1000 K) and data with temperature information close to 293~300K are preferred over data with no information, and (3) data with small *R*-value are preferred over data with large *R*-value or no information.

Lattice parameters are first investigated for elementary substances and then for binary oxides. In addition to the mean error (ME), the mean absolute error (MAE) and root mean square error (RMSE) are also evaluated. Outlier values are of interest because an approximation with somewhat large ME with less chance of an extremely large error could be more preferable than another with a smaller ME but gives widely off values in occasional cases. The largest positive and negative errors are also assessed for this reason. The dimensionality of the crystal is expected to strongly affect errors in the lattice parameters. LD structures are defined to have relatively large spacing between atoms along one or more axis, in contrast to three-dimensional (3D) structures. Examples of the LD structures include molecular crystals (examples are crystalline I that consists of I_2 dimers and arsenolite As_2O_3), one-dimensional chain-like structures (examples are crystalline Te and montroydite HgO), and layered structures (examples are graphite C and litharge PbO). Results are tabulated for lattice parameters of 3D structures (*a*, *b*, and *c* combined), and lattice parameters of LD structures along spacing (LD-s, short for LD-spacing) and along no spacing (LD-nos, short for LD-no spacing).

1. Elementary substances

The coll code and structure type as defined in the ICSD, space group type, and

lattice parameters of elementary substances are given in Supplementary Table I. Calculation results for individual elementary substances for each approximation are given in Supplementary Tables II-VIII. The investigated elementary substances are one representative each for all elements other than noble gases, lanthanides (except La and Ce), Po and heavier elements, and elements that are gaseous at room temperature (H, N, O, F, Cl). Diamond and graphite allotropes are evaluated for C as an exception. LD structures are the following: As, Bi, and Sb (As structure type according to the ICSD, spacing along *c*), Br and I (I_2, along *a*, *b*, and *c*), graphite C (graphite(2H), along *c*), P (P(black), spacing along *b*), S (S_8(*Fddd*), along *a*, *b*, and *c*), Se (Se(beta), along *a*, *b*, and *c*), and Te (Se(gamma), along *a* and *b*). There are 51 3D elementary substances and 153 lattice parameters in total. In addition, there are 10 LD elementary substances, where U=0 in all cases, with 19 LD-s and 11 LD-ns lattice parameters, respectively. As a result, means are taken over 153, 19, and 11 lattice parameters for 3D, LD-s, and LD-nos, respectively. Magnetization is considered in Cr (antiferromagnetic), Co, Fe, Mn, and Ni (each ferromagnetic).

Table III compares errors between approximations for elementary substances. The ME and MAE results show that PBE is the closest to experimental values for 3D structures. However, this does not immediately suggest that PBE is the best approximation. The RMSE is smallest in PBED3 and PBEsol at 2.1% and 2.2%, respectively, and the value for PBE of 3.2% is about 1% larger. The RMSE of SCAN, which is 2.7%, is better than PBE but worse than PBEsol, Furthermore, the LD-s ME, MAE, and RMSE in PBE are much larger than the other approximations, which indicates that PBE does not describe LD structures well. This is an expected result for PBE that neglects van der Waals interactions. On the other hand, PBEsol and SCAN performs surprisingly well despite the fact that, unlike PBED3, it does not explicitly model van der Waals interactions as in PBE. Adding +U corrections consistently worsen MAE and RMSE, hence adding +U should be avoided when trying to reproduce the lattice parameters.

Table IV gives the largest positive and negative errors in each approximation for elementary substances. The PBE results are discussed first (Supplementary Table II). The eye-catching absolute error is the huge +31.3% in PBE and PBE(+U), which is the

c lattice parameter of Hg (U_{eff}=0). The error in lattice parameter *a*=*b* is moderate at 3.8 %. The experimental structure of Hg is a rhombohedral cell where the face-centered cubic (fcc) structure is compressed in the [111] direction. However, in PBE, the lattice gradually expands along the *c*-axis upon relaxation until the fcc structure is attained. Other PBE lattice parameters of 3D structures where the absolute error is more than 5% compared to the experimental value are: *c* of Cd (5.5%, hexagonal close-packed (hcp) structure), *a*=*b*=*c* of Ce (-8.3%, fcc structure), *c* of In (8.6%, tetragonal In structure), and *c* of Zn (5.1%, hcp structure). On the other hand, the largest absolute error in PBE and PBE(+*U*) in a LD structure is 27.8%, which is the *a* lattice parameter of Br (U_{eff}=0). The error in lattice parameter *a* of isostructural I is also similarly large at 26.8%. Br and I have the same structure type (I_2), which is a molecular crystal composed of dimers. The error in the lattice parameter *c* of graphite is as large as 19.3%. Other PBE lattice parameters of LD structures (U_{eff}=0 for all systems) where the error is more than 5% compared to the experimental values are (all are along directions with spacing): *b* of Br (-8.2%), *b* of P (7.9%), *a* and *b* of S (19.5% and 18.3%, respectively), and *b* and *c* of Se (22.6% and 5.5%, respectively). Errors exceeding 5% or more in PBE(+*U*) lattice parameters (Supplementary Table III) of 3D structures appear in *c* of Cd (U_{eff}=0), *a*=*b*=*c* of Cr (11.1%, body-centered cubic (bcc) structure), *c* of Hg (*U*=0), *c* of In (*U*$_{eff}$=0), *a*=*b*=*c* of Mn (15.2%, Mn(alpha)-Mn(*cI*58) structure), and *c* of Zn (-9.9%, hcp structure). Comparing PBE and PBE+*U*, the Ce lattice parameter error is reduced from -8.3% to -4.5%, but the absolute errors of Mn, and Zn have increased significantly. In contrast, PBED3 lattice parameters (Supplementary Table IV) with absolute error exceeding 5% are very limited: *a*=*b*=*c* of Ce (-10.8%), *a*=*b*=*c* of Li (-5.0%, bcc structure), and *b* of Br (-10.7%). However, adding *U* (Supplementary Table V) increases the lattice parameters of 3D crystals with absolute error exceeding 5% to *a*=*b*=*c* of Ce (-7.8%), *a*=*b*=*c* of Cr (13.4%), *a*=*b*=*c* of Li (U_{eff}=0), *a*=*b*=*c* of Mn (12.7%), and *c* of Zn (-8.3%). Again, we see worsening in outlier values by addition of Hubbard *U*. On the other hand, the number of PBEsol lattice parameters (Supplementary Table VI) with absolute error exceeding 5% increases from PBED3 to: *c* of Cr (-12.3%), *a*=*b*=*c* of Ce (-11.1%), *a*=*b*=*c* of Mn (-5.3%), *a* and *b* of Br (6.5% and -13.5%, respectively), and *b* of I (-7.0%). Moreover, adding *U* (Supplementary Table VII) increases the number of such

lattice parameters of 3D crystals to $a=b=c$ of Ce (-8.2%), c of Co (9.9%), $a=b=c$ of Cr (7.7%), $a=b=c$ of Mn (12.9%), and c of Zn (-8.6%). SCAN lattice parameters with absolute errors more than 5% are $a=b=c$ of Ce (-10.2%), $a=b$ of Hg (14.7%), c of Hg (-12.6%), $a=b=c$ of Mn (-5.3%), b of Br (-9.4%), and a of I (6.7%). Looking at all seven approximations, some elementary substances frequently show up with relatively large absolute errors. Ce and Br typically have large absolute lattice parameter errors (the error of Ce in PBE+U is -4.5%), and the absolute error in at least one lattice parameter exceeds 7% in all approximations with Hubbard U in Cr ($a=b=c$), Mn ($a=b=c$), and Zn (c). The sign of the error changes from negative to positive by adding U in Cr and Mn for all approximations, thus tuning the value of U_{eff} may lead to a better reproduction of the lattice parameter in these two elementary substances.

In summary, although PBE shows the smallest ME and MAE in 3D structures, it does not perform well for LD structures, as expected. The MAE and RMSE for LD structures are small in PBED3, PBEsol, and SCAN. PBED3 or PBEsol, both without U, reproduces experimental lattice parameters well with fewer outliers having absolute error over 5%. The performance of PBEsol and SCAN is notable, given that these functionals do not include explicit van der Waals corrections.

2. Binary oxides

Table V compares errors between approximations for binary oxides with respect to experimental lattice parameters. There are 64 3D oxides and 192 lattice parameters total as well as 16 LD oxides with 25 LD-s and 23 LD-ns lattice parameters, respectively. Magnetization is not considered. Experimental data is given in Supplementary Tables IX and X and calculation results for individual oxides for each approximation are given in Supplementary Tables XI-XXIV. In contrast to results for elementary substances in Table III, PBED3 and PBEsol with and without Hubbard U as well as SCAN give smaller ME, MAE, and RMSE than PBE with and without U. Adding Hubbard U tends to increase the MAE and RMSE in all approximations. Therefore, PBED3, PBEsol, and SCAN appear to be reasonable choices simply on the basis of this table.

Table VI shows the largest positive and negative error in lattice parameter for

binary oxides. For PBE, the maximum absolute error for 3D crystals (Supplementary Table XI) is *c* of B_2O_3 in the 305 B_2O_3 prototype (5.8%), and the largest in LD crystals (Supplementary Table XII) is *c* of Cs_2O in the 102 Anti-$CdCl_2$(3R) prototype (18.3%, with spacing). There are more cases of maximum absolute error exceeding 10%, which are all found along directions with spacing: *c* of V_2O_5 in the 502 V_2O_5($P2_1/m$) prototype (13.1%), *c* of PbO in the 208 Litharge prototype, *b* of CrO_3 in the 601 CrO_3 prototype (11.8%), and *a* of MoO_3 in the 602 MoO_3 prototype (16.8%). Adding Hubbard *U* (Supplementary Tables XIII and XIV) does not result in a significant change in error in the crystals mentioned above. However, errors the lattice parameters of Ag_2O in the 101 Anti-CdI_2 prototype (LD, spacing along *c*) significantly worsens to *a*=*b*=11.1% and *c*=-8.9%. The absolute errors of other lattice parameters do not exceed 10%. In contrast, the largest error in PBED3 (Supplementary Tables XV and XVI) and PBED3(+*U*) (Supplementary Tables XVII and XVIII) is *c* of Cs_2O in the 102 Anti-$CdCl_2$(3R) prototype (5.6%, LD, direction with spacing, U_{eff}=0), followed by *c* of Bi_2O_3 in the 303 La_2O_3 prototype (-5.5% , 3D, *U*=0). These are the only lattice parameters where the absolute error exceeds 5% in PBED3; *a*=*b* of Ag_2O in the 101 Anti-CdI_2 prototype additionally becomes 5.0% in PBED3+*U*. On the other hand, the largest error in PBEsol (Supplementary Tables XIX and XX) is again *c* of Cs_2O in the 102 Anti-$CdCl_2$(3R) prototype (9.0%, LD, direction with spacing, U_{eff}=0), followed by *a* of MoO_3 in the 602 MoO_3 prototype (7.1%, LD, direction with spacing.) and *c* of Bi_2O_3 in the 303 La_2O_3 prototype (-6.3% , 3D, U_{eff}=0). Adding +*U* (Supplementary Tables XXI and XXII) increases the error of *a* of MoO_3 in the 602 prototype to 7.8% and the error of *c* of Ag_2O in the 101 Anti-CdI_2 prototype becomes to -5.2% (LD, direction with spacing). The absolute value of no other error exceeds 5% in PBEsol and PBEsol(+*U*). Lastly, only two lattice parameters have an absolute error larger than 5% in SCAN (Supplementary Tables XXIII and XXIV), which are *c* of Bi_2O_3 in the 303 La_2O_3 prototype (-6.0%) and *c* of Cs_2O in the 102 Anti-$CdCl_2$(3R) prototype (5.2%). These two lattice parameters are exactly those where the absolute error exceeded 5% in PBED3.

This overview of systems with large absolute errors (outliers) shows that, as in the case of elementary substances, specific lattice parameters of specific systems tend to give large errors and that PBED3 and SCAN tend to give slightly lower absolute errors

in outlier crystals compared to PBEsol. In summary, PBED3 and SCAN appear to be the best approximations when describing lattice parameters of binary oxides, while PBEsol performs reasonably well even for LD structures, as in the case of elementary substances.

B. Extent of relaxation from the experimental structure

Indices of relaxation LR_2, CR, and CR', which are defined in IIB, are obtained for binary oxides listed in Supplementary Tables IX and X and are listed in Supplementary Tables XXV-XXVII. The indices are zero by virtue of symmetry in some systems, namely prototypes 103 Anti-Fluorite-CaF_2, 104 CuO_2, 201 NaCl, 411 Fluorite-CaF_2, and 607 ReO_3, so these are not considered here. In addition, LR_2 is zero in cubic 301 Bixbyite-Mn_2O_3 and 307 As_2O_3 (*cF*80) prototypes, which are excluded from subsequent mean derivations. Table VII summarizes the means of LR_2, CR, and CR' over 3D and LD structures in the seven approximations. The mean LR_2 is 0.000 for all approximations in 3D systems, which show that the lattice deformation during relaxation is small. The ME of lattice parameters in 3D structures was 1.3% and 1.4% in PBE and PBE(+*U*), respectively, and between -0.2% and 0.4% in the other approximations (Table V). Therefore, the deformation of lattice parameters of 3D structures during relaxation is almost isotropic in all approximations, although the amount in PBE and PBE+*U* is much larger than the other approximations. On the other hand, the mean LR_2 of LD systems is 0.010 and 0.014 in PBE and PBE(+*U*), respectively, which is an order of magnitude larger than the other approximations. This result is consistent with the anisotropic relaxation in LD systems for PBE and PBE(+*U*) that is shown in Table V. The means of CR and CR' shows a consistent trend to decrease in the order of PBE and PBE(+*U*), PBEsol and PBEsol(+*U*), PBED3 and PBED3 (+*U*), and SCAN. Therefore, SCAN best reproduces the experimental internal coordinates.

C. Formation enthalpy and Gibbs free energy

The relation between experimental formation enthalpy $\Delta H_{f(exp)}$, or Gibbs free energy $\Delta G_{f(exp)}$ at 298 K versus calculated formation enthalpy $\Delta H_{f(calc)}$ or Gibbs free energy $\Delta G_{f(calc)}$ is considered in this section. Firstly, the vibrational contributions to the

formation enthalpy and Gibbs free energy are discussed. The vibrational contribution to the enthalpy with respect to the formation energy at 0K excluding vibrational effects, ΔH_f^{vib}, and the corresponding value for Gibbs free energy, ΔG_f^{vib}, for selected systems are listed in Table VIII. The change in the Gibbs free energy when the vibrational contribution is accounted for in the reference O_2 gas only, $\Delta G_f^{vib,O}$, is also shown. The vibrational contribution to the formation enthalpy is very small overall, and the largest contribution is 0.06 eV/atom in BeO. This contribution comes mainly from the zero point energy of BeO (0.11 eV/atom). The effect of vibrational contribution other than zero point energy is very small in BeO; the difference between Gibbs free energies at 0K and 300K is only 0.01 eV/atom. On the other hand, the contribution is larger in systems with weaker bonds. The largest difference between Gibbs free energies at 0K and 300K among the systems shown in Table VIII is PbO at 0.05 eV/atom.

There is a systematic, sizable contribution of 0.13 to 0.22 eV to the formation Gibbs free energy. Most of the contribution comes from O_2 gas since the absolute value of ΔG_f^{vib}-$\Delta G_f^{vib,O}$ is typically less than 0.05 eV, although it is 0.09 eV/atom in BeO. In summary, the vibrational contribution to the formation enthalpy and the vibrational contribution other than O_2 to the formation Gibbs free energy is expected to be less than 0.1 eV/atom.

Next we compare $\Delta H_{f(calc)}$ and $\Delta G_{f(calc)}$ against $\Delta H_{f(exp)}$ and $\Delta G_{f(exp)}$. Based on the aforementioned results for selected oxides, vibrational contributions are neglected here except for the contribution from O_2 when calculating $\Delta G_{f(calc)}$. The experimental data is obtained from the NIST-JANAF Thermochemical Tables (4^{th} edition) [91], CODATA Key Values for Thermodynamics [92], and Thermochemical Data of Elements and Compounds [93]. On the computational side, we use the low temperature polymorph of the cation elementary substance and the O_2 gas as reference states. The cation reference state is shown in Supplementary Table I. $\Delta H_{f(calc)}$ is estimated by using the 0 K, 0 GPa total energy of the electron system for the cation elementary substance, its oxide, and O_2 molecules. On the other hand, $\Delta G_{f(calc)}$ is obtained with respect to the 0 K, 0 GPa total energy of the electron system for the cation elementary substance and its oxide as well as the Gibbs free energy of O_2, which is the 0 K, 0 GPa total energy of the electron system plus the calculated zero-point energy and entropic contribution in O_2

using the experimental bond length (1.21 Å) and vibration frequency (1580.19 cm^{-1}) [94], which amounts to -0.22 eV/atom at room temperature.

Figures 4 and 5 are plots of $\Delta H_{f(calc)}$-$\Delta H_{f(exp)}$ versus $\Delta H_{f(exp)}$ and $\Delta G_{f(calc)}$-$\Delta G_{f(exp)}$ versus $\Delta G_{f(exp)}$, respectively. Individual values of $\Delta H_{f(exp)}$, $\Delta H_{f(calc)}$, $\Delta H_{f(calc)}$-$\Delta H_{f(exp)}$, $\Delta G_{f(exp)}$, $\Delta G_{f(calc)}$, and $\Delta G_{f(calc)}$-$\Delta G_{f(exp)}$ are given in Supplementary Tables XXVIII-XXXI. The horizontal lines show the mean average of $\Delta H_{f(calc)}$-$\Delta H_{f(exp)}$, and $<\Delta H_{f(calc)}$-$\Delta H_{f(exp)}>$ (Fig. 4), and of $\Delta G_{f(calc)}$-$\Delta G_{f(exp)}$, and $<\Delta G_{f(calc)}$-$\Delta G_{f(exp)}>$ (Fig. 5), respectively, over all considered systems. Table IX shows the ME, MAE, and RMSE of $\Delta H_{f(calc)}$-$\Delta H_{f(exp)}$ and $\Delta G_{f(calc)}$-$\Delta G_{f(exp)}$ for each approximation**.** The SCAN results are significantly different form the other approximations. The ME of $\Delta H_{f(calc)}$-$\Delta H_{f(exp)}$ is only 0.01 eV whereas the ME ranges between 0.15 to 0.24 eV in the other approximations, and the RMSE is slightly larger than one-half of the other approximations. On the other hand, the ME of $\Delta G_{f(calc)}$-$\Delta G_{f(exp)}$ by SCAN is negative at -0.04eV, while the MEs are 0.10 to 0.19 eV in the other approximations. Again, the RMSE is small at 0.07 eV compared to the other approximations that range between 0.11 to 0.13 eV. Aside from $<\Delta G_{f(calc)}$-$\Delta G_{f(exp)}>$ of SCAN, the MEs are all positive, which indicates that the calculated formation enthalpy and Gibbs free energy tends to overestimate respective experimental values. The discrepancy between $\Delta H_{f(calc)}$-$\Delta H_{f(exp)}$ and $<\Delta H_{f(calc)}$-$\Delta H_{f(exp)}>$ as well as $\Delta G_{f(calc)}$-$\Delta G_{f(exp)}$ and $<\Delta G_{f(calc)}$-$\Delta G_{f(exp)}>$ of most systems (the error) are within 0.2 eV, although the largest maximum and minimum errors are 0.16 and -0.19 eV, respectively, in SCAN. For approximations other than SCAN, the outlier results are always the same regardless of the approximation, such as PbO (both 207 Litharge and 208 Massicot prototypes), Al_2O_3 (302 Corundum-Al_2O_3 prototype), and Bi_2O_3 (309 Bi_2O_3 prototype). The effect of adding Hubbard *U* depends on the system. ZnO (202 Wurtzite-ZnS(2H)) has positive $(\Delta H_{f(calc)}$-$\Delta H_{f(exp)})$-$<\Delta H_{f(calc)}$-$\Delta H_{f(exp)}>$ and $(\Delta G_{f(calc)}$-$\Delta G_{f(exp)})$-$<\Delta G_{f(calc)}$-$\Delta G_{f(exp)}>$ without *U* but negative with *U*, and is the other way around in CrO_3 (601 CrO_3). Although Zn and Ga have fully occupied 3*d* orbitals, the effect of adding *U* is significant; the calculated enthalpy differs by 0.2 and 0.3-0.4 eV, respectively, between with and without *U*.

In summary, the SCAN meta-GGA consistently gives excellent formation

enthalpy and Gibbs free energy, while those derived from calculations using other GGA approximations tend to consistently overestimate experimental data. PBED3 and PBEsol show ~0.05 to 0.1 eV smaller errors than PBE for both with and without Hubbard *U*. The systematic error in GGA has been addressed previously. For instance, Wang *et al*. [95] proposed a correction of 1.36 eV per O_2 on the basis of six non-transition metal cation oxides, while Stevanović devised the FERE scheme where 252 enthalpies of formation were used to derive a correction per atom for 50 elements [87].

D. Relative energies between prototypes

1. Monovalent cation oxides

There is not much difference between results using different approximations, as shown in Fig. 6 and Supplementary Tables XXXII-XXXVIII. Hubbard *U* is non-zero in Cu, Ag, and Au only. The 104 Cu_2O prototype (cuprite structure) is favored with all approximations for Cu_2O, Ag_2O, and Au_2O. Cations and O are two- and four-fold coordinated, respectively, in this structure. Cu_2O and Ag_2O are known as stable compounds, but Au_2O is not; the only known gold oxide with a crystallographically well-characterized structure and sufficient stability under ambient conditions is Au_2O_3 [96]. On the other hand, Cs_2O and Tl_2O stabilize in the 101 Anti-CdI_2 and 102 Anti-$CdCl_2$(3R) prototypes. These are both layered structures where each layer consists of a monolayer of six-fold coordinated O sandwiched by three-fold coordinated cations. Tl_2O in the "anti-CdI_2 type structure" with Z=6 and space group type $R\bar{3}m$ (number 166) is reported [97], but this is not the same as any prototype considered in this study. Closing the gaps between layers in the 102 Anti-$CdCl_2$(3R) prototype results in the 103 Anti-Fluorite-CaF_2 prototype that is favored by Li_2O, Na_2O, and K_2O (also see Fig. 1). Rb_2O is slightly metastable by 5 meV/atom compared to the 102 Anti-$CdCl_2$(3R) prototype in PBE, while Rb_2O is stable in the 103 Anti-Fluorite-CaF_2 prototype in other approximations. As the cation size increases from Li toward Cs and Tl, the energetic benefit of increased coordination number by taking the 103 Anti-Fluorite-CaF_2 prototype would become less preferable compared to the cost in retaining the rigid coordination of the cubic 103 Anti-Fluorite-CaF_2 structure with fixed internal

coordinates. One may be tempted to use electronegativity to explain that a layered structure is stable in CsO_2 but not in lighter alkaline metal oxides as the Cs-O bond would become very ionic and the ionic charge of Cs in Cs_2O becomes more positive compared to other group 1 counterparts, and therefore Cs layers on both sides should repel each other. However, this electronegativity argument does not hold for Tl as Tl is much more electronegative than group 1 elements but still prefers a layered structure.

2. Divalent cation oxides

As in the monovalent case, there is not much difference between results using different approximations, as shown in Fig. 7 and Supplementary Tables XXXIX-XLV. Hubbard U is non-zero in Zn only, but the relative energies between prototypes are almost identical with or without U despite the large value of U_{eff} = 5 eV. The ground states are the same in all approximations: the 201 NaCl prototype in MgO, CaO, SrO, BaO, and CdO, 202 Wurtzite-ZnS(2H) followed closely (6-8 meV/atom) by 203 Sphalerite-ZnS(*cF*8) (zincblende structure) in BeO and ZnO, 205 HgO with 206 HgS barely metastable (1-2 meV/atom) in HgO, and 208 Litharge in SnO and PbO.

There is a clear rule regarding stable prototypes and cation size: smaller and more covalent cations (group 2 Be and group 12 Zn) tend to favor four-fold coordinated prototypes, 202 Wurtzite-ZnS(2H), 203 Sphalerite-ZnS(*cF*8), and 204 BeO(*tP*8), while the six-fold coordinated prototype 201 NaCl is stable in intermediately sized cations (group 2 Mg, Ca, Sr, Ba and group 12 Cd). However, in CdO, the 202 Wurtzite-ZnS(2H) prototype with four-fold coordinated cations is only 6 meV/atom metastable compared to the six-fold coordinated ground state 201 NaCl prototype in PBE. This difference increases by an order of magnitude in PBED3, PBEsol, and SCAN. A combined experimental and theoretical study on the pressure-induced wurtzite to rocksalt structure transition in $Cd_xZn_{1-x}O$ suggests that the zero pressure phase is wurtzite at x<0.67 and rocksalt at x>0.67 [98]. The ratio of energy differences between 201 NaCl and 202 Wurtzite-ZnS(2H) prototypes in ZnO and CdO is expected to be about 2:1, assuming a linear change with x and a transition concentration of x = 2/3 threshold. The absolute energy differences are 149 and 6 meV/atom in PBE, 102 and 63 meV/atom in PBED3, 110 and 56 meV/atom in PBEsol, and 112 and 74 meV/atom in SCAN, respectively. The +U corrections change the relative phase stability in ZnO only

slightly, which means that the energy differences in PBED3, PBED3(+*U*), PBEsol, PBEsol(+*U*), and SCAN are reasonable but not in PBE and PBE(+*U*). The six-fold coordinated 209 Nickeline-NiAs prototype never becomes the most stable prototype but is second most stable in CaO, SrO, and BaO, and the energy difference between 201 NaCl and 209 Nickeline-NiAs decreases as the cation size increases in alkaline earth metal oxides. Hg prefers two-fold coordination and therefore forms chain structures (prototypes 205 HgO and 206 HgS). SnO and PbO stabilizes in layered structures (207 Massicot and 208 Litharge) as Sn^{2+} and Pb^{2+} has "lone pairs" of valence *s*-electrons that interact weakly between layers of SnO or PbO [99].

The following analysis demonstrates that the choice of approximation determines the interlayer distance of two-dimensional structures. The tetragonal 208 Litharge structure has four atoms in the conventional unit cell. There are two lattice parameters, *a* and *c*, and one internal coordinate, *u*. The space group type is *P*4/*nmm* (number 129), cations occupy 2*c* sites with coordinate triplets (0, 1/2, *u*) and (1/2, 0, $\overline{u}$), and anions occupy 2*a* sites with coordinate triplets (0, 0, 0) and (1/2, 1/2, 0). Therefore, the interlayer distance is *c* and the thickness of each layer is 2*uc*. Tables XI and XIII shows information on *a*, *c*, *c*/*a*, *u*, and 2*uc* for SnO and PbO, respectively. The layer thickness agrees within 0.01Å and 0.02 Å for SnO and PbO, respectively, between experimental data, PBE, PBED3, PBEsol, and SCAN. In contrast, there is one order of magnitude larger discrepancy in the lattice parameter *c*: the result from PBE is 0.5Å and 0.2 Å larger than experimental data for SnO and PbO, respectively, while *c* from PBED3, PBEsol, and SCAN differ from experimental data by 0.1 Å or less. This means that the choice of approximation affects the interlayer distance but not the thickness of the layers in "lone pair" systems.

3. Trivalent cation oxides

The relative energies between stable and slightly metastable prototypes do not differ much between approximations, but there are some distinct differences (Fig. 8 and Supplementary Tables XLVI-LII). Hubbard *U* is non-zero in Ga and La only.

We first investigate trends in Al_2O_3, Ga_2O_3, In_2O_3, Sc_2O_3, Y_2O_3, and La_2O_3. The ionic radius of the cation increases from left to right, with the exception of In^{3+} and

Sc^{3+} where Shannon's ionic radius [100] is larger in the former compared to the latter. Compared to the 301 Bixbyite-Mn_2O_3 prototype, 302 Corundum-Al_2O_3 becomes increasingly stable toward Al_2O_3 whereas 303 La_2O_3 stabilizes more toward La_2O_3. In Al_2O_3, the α-phase (302 Corundum-Al_2O_3 prototype) is most stable. The θ-phase is used as the Pt atom support in CO [101] and NO [102] oxidation catalysts. has applications in catalyst supports. This phase is slightly metastable by 9 to 39 meV/atom. Five polymorphs of Ga_2O_3 are experimentally known, which are α- (301 Bixbyite-Mn_2O_3 prototype), β- (304 Ga_2O_3 prototype), γ-, δ-(302 Corundum-Al_2O_3 prototype), and ε-Ga_2O_3. Experiments show that the β-Ga_2O_3 structure is stable under ambient conditions [103,104], which is in accordance with our calculations. The α-Ga_2O_3 phase is reported not in the ICSD but elsewhere and therefore indicated with a red arrow in Fig. 8. 301 Bixbyite-Mn_2O_3 is most stable in In_2O_3, Sc_2O_3, and Y_2O_3 in all approximations. La_2O_3 is known to be stable in the 303 La_2O_3 prototype, or A-type structure in rare earth sesquioxide nomenclature, at ambient conditions. The 301 Bixbyite-Mn_2O_3 prototype, or C-type rare earth sesquioxide structure, is stable in late lanthanide sesquioxides but is not obtained when heating La_2O_3 at ambient pressure [105]. Our computational results show that the 303 La_2O_3 prototype is the most stable La_2O_3 structure in PBED3, PBEsol, and SCAN but is barely metastable (≤ 5 meV/atom) in PBED3+*U* and PBEsol+*U* and is metastable in PBE and PBE+*U* (24 and 31 meV/atom, respectively).

B_2O_3 takes a unique structure (305 B_2O_3 prototype) arising from covalent bonding between B and O where B form sp^2 hybrid orbitals and become three-fold coordinated, and O is two-fold coordinated with the bond angle about 130 degrees. This structure is predicted to be stable with any approximation; the other structures are much higher in energy and do not appear in the energy range of Fig. 8.

As_2O_3, Sb_2O_3, and Bi_2O_3 have "lone pair" *s*-electrons [106] and thus forms phases different from group 3 and group 13 (except B) sesquioxides. However, prototypes 301 Bixbyite-Mn_2O_3, 306 As_2O_3, 307 As_2O_3(*cF*80), 308 Sb_2O_3, and δ-Bi_2O_3 (the high temperature form of Bi_2O_3, not considered as a prototype in this study due to existence of partial occupancy on the anion sites, that is known as the fastest solid-state oxygen ion conductor at elevated temperature [107]) can be considered as variations of

the fluorite structure with various anion defects [106]. In other words, variations of the defective fluorite structure appear in almost all of the ternary cation sesquioxides. As_2O_3 has two crystalline polymorphs: monoclinic claudetite (306 As_2O_3 prototype) and cubic arsenolite (307 As_2O_3(*cF*80) prototype). A Research Council Committee in the USA claims that the arsenolite phase is known to be stable below –13 °C [108] while Wells states that the low temperature form is the claudetite phase and transitions to the arsenolite phase at 110 °C [109]. Our calculations find that the claudetite phase is more stable at 0 K than the others by 2-10 meV/atom in all approximations. Sb_2O_3 is known in two forms: cubic α-Sb_2O_3 (senarmontite, 307 As_2O_3(*cF*80) prototype) and orthorhombic β-Sb_2O_3 (valentinite, 308 Sb_2O_3 prototype). The low temperature form is valentinite that transforms to senarmontite at 606 °C [109]. The valentinite phase is the lowest energy structure in all approximations. Six polymorphs of Bi_2O_3 are experimentally known, which are monoclinic α- (stable at ambient conditions, 309 Bi_2O_3 prototype), tetrahedral β- (310 Bi_2O_3(*tP*20) prototype), cubic γ-, cubic δ-, orthorhombic ε- (308 Sb_2O_3 prototype), and triclinic ω-Bi_2O_3. Moreover, a bixbyite structure-related η-Bi_2O_3 phase is theoretically predicted to be dynamically stable [110]. Calculations from all approximations point out that Bi_2O_3 is most stable in the α-Bi_2O_3 phase and β- and ε-Bi_2O_3 are both metastable within 47 meV/atom from α-Bi_2O_3.

4 Tetravalent cation oxides

There is much difference between approximations in the order of stability of tetravalent oxide prototypes (Fig. 9 and Supplementary Tables LIII-LIX). The Hubbard *U* is non-zero in Ti, Zr, and Hf only.

SiO_2 is notable for its rich variety of polymorphs. Polymorphs that appear in a temperature-pressure phase diagram up to 3300 K and 20 GPa are quartz, tridymite, cristobalite, coesite, and stishiovite. Among these, quartz, tridymite, and cristobalite have low temperature (α-) and high temperature (β-) forms [111]. The reversible displacive transition between low and high temperature forms in quartz is called quartz inversion and happens instantaneously around 846 K [112]. Tridymite undergoes a number of transitions between about 380 to 440 K and cristobalite shows a transition at 535 K [113]. Low temperature (α-) quartz is the stable phase at ambient temperature and

pressure. Heating at ambient temperature changes the most stable polymorph to β-quartz, β-tridymite, and β-cristobalite, while applying pressure at room temperature results in transition of the most stable modification to coesite and then stishiovite [114]. Additional high temperature and ultrahigh pressure (>20 GPa) phases [115] are a disordered NiAs-type structure, a $CaCl_2$-type phase, seifertite [116], and a pyrite-type phase. Other known phases include keatite [117] and moganite, which has low and high temperature forms (space group types *I*2/*a* and *Ibam*, numbers 15 and 72, respectively) with a transition point around 570 K and can be regarded as quartz that is Brazil twinned along (101) at the unit cell scale [118]. Many of the polymorphs can be derived from a single bcc lattice framework (space group type $Im\bar{3}m$, number 229) but with different ordering patterns and deformations. Si occupy 2*a* sites while O occupy *6b* sites. The stishovite phase can be obtained when all Si sites are occupied and 1/6 of O sites are occupied, β- quartz and coesite when 2/3 and 1/9 of Si and O sites are occupied, respectively, and β-tridymite and β-cristobalite when 1/2 and 1/12 of Si and O sites are occupied, respectively [114]. The high pressure phases have higher occupancies than low pressure phases. Stishiovite becomes stable above approximately 10 GPa [111]. The stable region of β-quartz extends up to around 4 GPa while β-tridymite and β-cristobalite and can be stable only under about 0.15 and 0.6 GPa, respectively, thus β-quartz can be regarded as a high-pressure phase compared to β-tridymite and β-cristobalite. The experimental formation enthalpies at 298K of tridymite, cristobalite, coesite, stishovite, and moganite compared to quartz at 298K are 11 [119], 7 [91] or 9 [120] , 17 [120] or 18 [119], 171 [120], and 12 [121] meV/atom, respectively.

This study investigates α-quartz (415 Quartz, low prototype), α-cristobalite (417 Cristobalite-alpha), coesite (418 Coesite), stishiovite (401 Rutile-TiO_2), moganite (416 Moganite), the $CaCl_2$-type phase (413 $CaCl_2$), seifertite (406 PbO_2-alpha), and the modified fluorite-type or pyrite-type (414 PdF_2(*cP*12)) phase. The α-tridymite phase is not considered as many modifications have been reported [111] and there is no consensus on its structure. The existence of many possible modifications in α-tridymite is consistent with the numerous transitions found upon heating of tridymite [113]. The calculated formation energies increase in the order of α-quartz, coesite, stishiovite, and seifertite in all approximations. PBED3, PBEsol, and SCAN gives α-quartz,

α-cristobalite, coesite, and moganite within a 20 meV/atom range that is consistent with experimental reports [91,119,120]. However, the formation energy of stishiovite compared to α-quartz is 88 and 60 meV/atom in PBED3 and PBEsol, respectively, which is about 0.1eV less than the experimentally reported value. On the other hand, in PBE stishiovite is 185 meV/atom less stable than α-quartz, but the lowest energy structure is α-cristobalite that is 8 meV/atom more stable. SCAN shows a good compromise, where the calculated formation energy of stishiovite is 127 meV/atom, which comes roughly midway between experiment and PBED3, and the lowest energy structure is α-quartz, in line with experimental observations. These results suggest that PBED3, PBEsol, and SCAN give reasonable formation energies in low pressure phases but PBED3 and PBEsol severely underestimate energies of stishiovite and higher pressure phases.

A transition sequence similar to high pressure phases of SiO_2 is found in GeO_2 [115,122] and SnO_2 [123,124]. The ambient condition phase of GeO_2 and SnO_2 is the 401 Rutile-TiO_2 prototype, while increasing pressure and temperature results in transformation to the 413 $CaCl_2$, 406 PbO_2-alpha (α-PbO_2-type), and then the 414 PdF_2 (*cP*12) prototype (modified fluorite-type or pyrite-type). This sequence is recovered by all approximations in our calculations except that the symmetry of 413 $CaCl_2$ increases and becomes exactly the same as 401 Rutile-TiO_2. The 401 Rutile-TiO_2 to 406 PbO_2-alpha transition pressure of SnO_2 is discussed in Section 6.

The α-quartz structure (415 Quartz,low prototype) of GeO_2 is eliminated in PBED3, PBEsol, and SCAN because of excessive relaxation in internal coordinates. Fig. 10 shows how SiO_4 and GeO_4 octahedra relax from the original 415 Quartz-low prototype. The PBE SiO_2 relaxed structure, the original prototype, and PBE and PBED3 GeO_2 relaxed structure are shown from two directions. The amount of relaxation is different although the overall structure is kept intact. The SiO_4 and GeO_4 octahedra tilt in opposite directions from the experimental reported prototype, and the amount of relaxation is smaller in SiO_2, which results in a smaller *CR* value (Section 2). The two GeO_2 structures are close to the cutoff threshold of 0.25 Å in this study, and the PBED3 structure is eliminated while the PBE structure is barely accepted. Determination of the threshold is a difficult issue, but a value much larger than 0.25 Å appears to be too

excessive. Had we decided to not eliminate the 415 Quartz-low prototype of GeO_2, the relative energies against the 401 Rutile-TiO_2 prototype in PBED3, PBEsol, and SCAN are 115, 141, and 119 meV/atom, respectively, which are more than two times larger than 49 meV/atom in PBE.

PbO_2 has two major polymorphs, which are orthorhombic α-PbO_2 in the 406 PbO_2-alpha prototype and tetragonal β-PbO_2 in the 401 Rutile-TiO_2 prototype [125]. Applying pressure to α-PbO_2 results in transition to 413 $CaCl_2$, 414 PdF_2 (*cP*12), 404 Brookite-TiO_2 (HfO_2), and then the 412 HfO_2 prototype in this order, whereas pressurizing β-PbO_2 results in reversible transformation to the 414 PdF_2(*c*P12) prototype [126]. ICSD data on the 411 Fluorite-CaF_2 prototype PbO_2 (ICSD coll code 77468) is removed from Fig. 9 as the crystal structure of cubic PbO_2 is now considered to be the 414 PdF_2 (*cP*12) prototype [126]. In addition, the cottunite-type PbO_2 [126,127] is actually the 412 HfO_2 prototype instead of the VO_2 structure as stated in the ICSD (ICSD coll codes 189977-189985). As a consequence, PbO_2 in 412 HfO_2 and 414 PdF_2 (*cP*12) prototypes are labeled with red arrows in Fig. 9. The calculated energy difference between α- and β-PbO_2 is within 5 meV/atom in all four approximations. The lowest energy prototype is β-PbO_2 in PBE and α-PbO_2 in in PBED3, PBEsol, and SCAN. PbO_2 in PBED3 and PBEsol are the only cases where reducing the tetragonal symmetry of the 401 Rutile-TiO_2 prototype to the octahedral 413 $CaCl_2$ prototype reduces the formation energy (2 meV/atom in both cases); however, the observed β-PbO_2 phase has tetragonal symmetry. Two as-yet-unreported prototypes, which are 404 Brookite-TiO_2(HfO_2) and 409 ZrO_2 (*oP*12), are metastable within 10 meV/atom from the lowest energy polymorph in PBED3 and PBEsol but not in PBE and SCAN. The relative energy of the 409 ZrO_2 (*oP*12) prototype against the lowest energy prototype is 5 meV/atom in PBE but is eliminated because the *CR* is marginally above the threshold (0.26 Å). The 409 ZrO_2 (*oP*12) prototype relaxes to the 406 PbO_2-alpha prototype in SCAN.

TiO_2 is one of the most important binary transition metal oxides because of its numerous applications [128,129]. There are three polymorphs at ambient conditions: rutile (401 Rutile-TiO_2 prototype), anatase (402 Anatase-TiO_2 prototype), and brookite (403 Brookite-TiO_2 (TiO_2) prototype). The brookite phase [130] is the most difficult to

form among these three, and the rutile phase is experimentally suggested to be slightly stable compared to the anatase phase [131-133] (0.02 eV/atom difference in NIST-JANAF tables [91]). Applying pressure to the anatase phase yields orthorhombic columbite-type TiO_2-II (406 PbO_2-alpha prototype) and monoclinic baddeleyite TiO_2-III (405 Baddeleyite-ZrO_2 (*mP*12) prototype) [134-136]. Other known phases are TiO_2(R) (407 VO_2 prototype) [137], TiO_2(B) (408 VO_2 (HT) prototype) [138], and TiO_2(H) [139].

Rutile (401 Rutile-TiO_2) is not the most stable polymorph with PBE, PBED3, PBEsol, and SCAN in our results. Instead, PBE, PBEsol, and SCAN calculations indicate that the anatase structure (402 Anatase-TiO_2) is most stable, and the brookite structure (403 Brookite-TiO_2 (TiO_2)) is most stable in PBED3. One possible reason is too delocalized 3*d* electrons in PBE. Forcing the rutile structure to be the lowest energy structure is possible by adding the empirical Hubbard *U* correction, as shown in our results regarding PBE+*U*, PBED3+*U*, and PBEsol+*U*. Another trick is using a hybrid functional with nonlocal Fock exchange mixing over 70% [140]. However, these computational results are at 0K and do not include finite temperature effects. Trail *et al*. calculated finite temperature effects from anharmonic vibrations and total energies including many-body effects using diffusion quantum Monte Carlo calculations for rutile, brookite, and anatase phases of TiO_2 [141]. Anharmonic contributions were based on the vibrational self-consistent field method [142] and PBEsol total energies were employed. The maximum difference in relative free energy of TiO_2 polymorphs between 0K and 300K is at most ~2 meV/atom in Trail *et al*. [141]. Therefore, when vibrational effects are accounted for, the relative energies in our work may change by few meV/atom, but probably not at a scale of few tens of meV/atom. According to Trail *et al*. [141], the ground state is anatase, and the relative difference in Helmholtz free energy between brookite and anatase slightly increases with increasing temperature. TIn contrast, the Helmholtz energy of rutile decreases compared to anatase with increasing temperature, making rutile the most stable above ~600 K. Our PBEsol energy difference between rutile and anatase TiO_2 is 14 meV/atom. This energy difference becomes zero at around 1000 K when the change in Helmholtz free energy with increasing temperature according to Trail *et al*. [141] is considered as a correction. A similar result

has been reported using a quantum Monte Carlo method and density functional perturbation theory with LDA [128]. From another point of view, the relative energy of anatase (402 Anatase-TiO_2), TiO_2-II (406 PbO_2-alpha) and TiO_2-III (405 Baddeleyite-ZrO_2 (*mP*12)) phases should increase in this order based upon experimental results when the pressure is increased; this is the case in PBE, PBE+*U*, and SCAN.

HfO_2 takes the 405 Baddeleyite- ZrO_2 (*mP*12) prototype at ambient conditions. Varying the temperature and pressure leads to formation of two orthorhombic structures (orthorhombic I, space group type *Pbca*, number 61 and orthorhombic II, space group type *Pnma*, number 62), a tetragonal structure (space group $P4_2/nmc$, number 137) and a cubic structure (411 Fluorite-CaF_2 prototype) [143-145]. We note that the internal coordinates for the Brookite-TiO_2 structure (space group type *Pbca*) of TiO_2 are significantly different from those of HfO_2 and ZrO_2, therefore are considered different prototypes (403 Brookite-TiO_2 (TiO_2) and 404 Brookite-TiO_2 (HfO_2), respectively). Moreover, both 407 VO_2 and 412 HfO_2 prototypes have space group type *Pnma* and same formula units in the conventional cell (four). Whether the experimentally observed tetragonal structure coincides with the 410 Zirconia-HT-ZrO_2 prototype is unknown. Our calculations show that the 405 Baddeleyite-ZrO_2 (*mP*12) prototype is the most stable structure except for PBE+*U* where it is degenerate within 1 meV/atom with the 401 Rutile-TiO_2 prototype. Prototypes not experimentally found but are metastable within 30 meV/atom are 401 Rutile-TiO_2 and 413 $CaCl_2$ (PBE+*U*, PBED3+*U*, PBEsol+*U*), 402 Anatase-TiO_2 (PBE, PBE+*U*), 406 PbO_2-alpha (PBE, PBE+*U*, PBED3+*U*, PBEsol+*U*), 409 ZrO_2 (*oP*12) (all approximations). In particular, only 409 ZrO_2 (*oP*12) appears in this list with PBED3, PBEsol, and SCAN.

More polymorphs are experimentally reported for ZrO_2. The structure under ambient conditions is 405 Baddeleyite-ZrO_2 (*mP*12) prototype. The tetragonal 410 Zirconia-HT-ZrO_2 and cubic 411 Fluorite-CaF_2 structures can be obtained by heating, and three orthorhombic structures can be obtained by applying pressure (orthorhombic-I, II, III, in order of increasing pressure) [146]. The 409 ZrO_2 (*oP*12) prototype was proposed as the structure of orthorhombic-I [147] but Leger *et al*. rejected this claim and found that its space group type is *Pbca* and the lattice parameters are close to those of the Brookite-TiO_2 structure, which also has the *Pbca* space group type. Our

calculations corroborate Leger *et al.*'s finding as the 404 Brookite-TiO_2 (HfO_2) prototype has lower energy than the 409 ZrO_2 (*oP*12) prototype in all approximations. The orthorhombic-II phase is the 412 HfO_2 prototype. On the other hand, our calculations consistently show that the 405 Baddeleyite-ZrO_2 (*mP*12) prototype is the lowest energy structure. Low energy structures within 30 meV/atom of the 405 Baddeleyite-ZrO_2 (*mP*12) prototype other than the experimentally found 409 ZrO_2(*oP*12) prototype, are 401 Rutile-TiO_2 and 413 $CaCl_2$ (PBE+*U*), 402 Anatase-TiO_2 (PBE, PBE+*U*), 404 Brookite-TiO_2 (HfO_2) (all approximations), and 406 PbO_2-alpha (PBE, PBE+*U*).

5 Pentavalent cation oxides

Results are given in Fig. 11 and Supplementary Tables LX-LXVI. Hubbard *U* is non-zero in all cations. The ground state structure of V_2O_5 at ambient conditions is orthorhombic α-V_2O_5 (501 V_2O_5 prototype), and increasing pressure yields monoclinic β-V_2O_5 (502 V_2O_5 ($P2_1/m$) prototype) and monoclinic δ-V_2O_5 (503 Sb_2O_5 prototype), in this order [148]. Orthorhombic γ'-V_2O_5 (space group *Pnma*) [149] is known as a metastable phase. Our calculations show that in all approximations α-V_2O_5 is most stable, followed by β-V_2O_5 and δ-V_2O_5. Many modifications are reported for Nb_2O_5, which include R-, P- (or η-), M- (or β-, α'-) N-, H- (or α-), B-(or ζ-), T- (or γ-), and TT- (or δ-, γ'-) Nb_2O_5 (Section 9.15.2.6.1 in Landolt-Börnstein, new series, group III, volume 17, subvolume g) [150]. Kodama *et al*. suggests that the stable structure under ambient conditions is P-Nb_2O_5, which becomes B-Nb_2O_5, then H-Nb_2O_5 upon heating [151,152]. Only the monoclinic B- (ζ-) Nb_2O_5 is considered as a prototype (503 Sb_2O_5) in this study. The tetragonal P-(η-)Nb_2O_5 is not found in the ICSD and one site in H-(α-)Nb_2O_5 is partially occupied [153], therefore these are excluded from our calculations. PBED3, PBED3+*U*, PBEsol, PBEsol+*U*, and SCAN give the experimentally reported 503 Sb_2O_5 as the lowest energy prototype and at least 12 meV/atom more stable than the 501 V_2O_5 prototype, while PBE and PBE+*U* states that the 501 V_2O_5 prototype is slightly stable by 8 and 1 meV/atom, respectively, than 503 Sb_2O_5. The crystal structure of Ta_2O_5 at ambient pressure is difficult to solve as the multiplicity fluctuates between 11 to 14 depending on the synthesis conditions and

single crystals are very difficult to obtain [154]. High pressure phases of Ta_2O_5 include B- and Z-Ta_2O_5 [155]. Our calculations on Ta_2O_5 yield similar results to those of Nb_2O_5, where the experimentally obtained (albeit high pressure) B-Ta_2O_5 structure (503 Sb_2O_5 prototype) is stable than the as-yet-unreported 501 V_2O_5 prototype in PBED3, PBED3+*U*, PBEsol, PBEsol+*U*, and SCAN, which is the same trend as in Nb_2O_5.

6. Hexavalent cation oxides

Results are given in Fig. 12 and Supplementary Tables LXVII-LXXIII. Hubbard *U* is non-zero in all systems. In CrO_3, the experimentally reported 601 CrO_3 prototype appears as the unique or lowest energy prototype in all approximations. Four phases of anhydrous MoO_3 are reported in the literature, which are orthorhombic α-MoO_3 (602 MoO_3 prototype) that is thermodynamically stable under ambient conditions, metastable monoclinic β-MoO_3 and β'-MoO_3 (605 WO_3 (*mP*32) prototype), and high-pressure monoclinic MoO_3–II [156]. WO_3 has numerous polymorphs at ambient pressure: upon heating, the monoclinic ε-WO_3 phase (603 WO_3 (*mP*16) prototype) transitions to the triclinic δ -WO_3 phase (604 WO_3 (*aP*32) prototype) at -25 °C, then to the monoclinic γ-WO_3 phase (605 WO_3 (*mP*32) prototype) at 20-30 °C, orthorhombic β-WO_3 phase (606 WO_3 (HT) prototype) at 330 °C, and finally to the tetragonal α-WO_3 phase at 740 °C (Ref. [157] and within). These WO_3 polymorphs have structural distortions (rotation of WO_6 octahedra and displacement of W from the octahedron center) from the cubic ReO_3 structure (607 prototype) found in the tungsten bronze framework, which is the perovskite structure but without atoms in the A site [158]. Calculations on MoO_3 indicate that the α-MoO_3 phase is never the most stable structure but the ε-, δ-, γ-, and β-WO_3 phases, whose energies are similar within 3 meV/atom, are instead more stable. The α-MoO_3 phase is 17-51 meV/atom less stable than the most stable prototype. For WO_3, the latter four phases are stable and lie within 1 meV/atom in PBE, PBE+*U*, PBEsol, and SCAN. However, β-WO_3 is clearly stable compared to ε-, δ-, and γ-WO_3 in PBED3 and PBED3+*U*. The ReO_3 structure (607 ReO_3 prototype) is metastable compared to ε-, δ-, γ-, and β-WO_3 phases in WO_3 by at least 12 meV/atom, which shows that distortions from the defective perovskite framework lower the energy in WO_3.

E. Phase transition pressure

Prediction of the phase transition pressure is one criterion to evaluate the performance of an approximation. For instance, Cu_2O is known to transition from the cuprite structure (104 Cu_2O prototype) to an intermediate hexagonal phase at 10 GPa, and then transition to the 102 Anti-$CdCl_2$(3R) prototype at 13 to 18 GPa [159]. Ag_2O transitions from the cuprite structure (104 Cu_2O prototype) to the intermediate hexagonal phase found in Cu_2O at 0.4 GPa [159]. ZnO transitions from the 202 wurtzite-ZnS(2H) prototype to the rocksalt structure (201 NaCl prototype) around 9 GPa [160-163] and reverts to the 202 Wurtzite-ZnS(2H) prototype upon decompression around 2 GPa [162]. SnO_2 transitions from the 401 Rutile-TiO_2 prototype to the 413 $CaCl_2$ prototype at 11.8 GPa under hydrostatic conditions, the α-PbO_2-type phase (406 PbO_2-alpha prototype) starts to appear under non-hydrostatic conditions above 12.5 GPa, and finally transitions to a modified fluorite-type phase (414 PdF_2(*cP*12) prototype) above 21 GPa [123]. Upon decompression, the internal coordinate *u* of O in 8*c* sites of the modified fluorite phase significantly increases at 14.2 GPa, indicating that this phase becomes no longer stable below this pressure.

Among the above, two pressure-induced phase transitions are investigated in this study, which are wurtzite to rocksalt structure in ZnO and α-PbO_2-type to modified fluorite-type structure in SnO_2. Experimental information on hysteresis is available in these transitions [123,162], which means that the thermodynamic transition pressure is likely to lie between the transition pressures upon compression and decompression. Calculated transition pressures are listed in Table XII along with experimental values [98,123,160-166]; the local density approximation (LDA) and LDA+*U* are compared in addition to the six approximations in this section.

The experimental temperature (*T*, unit K) dependence on the transition pressure (*P*, unit GPa) of ZnO is P=8.0-0.0023T in Inoue [165] and P=6.7-0.0012T in Kusaba *et al*.[164]. The change in transition pressure in the two relations are 0.69 and 0.36 GPa, respectively, between 0K and 300K and 2.3 and 1.2 GPa, respectively, between 0K and 1000K. The *P*-*T* relation is nonlinear in the LDA results by Seko *et al.* [167]; with vibrational effects, the transition pressure is 7.65 GPa at 0 K but decreases to about 7.4

GPa at 300 K and about 5.0 GPa at 1000 K. The 0K transition pressure increases by 1 GPa to 8.65 GPa when vibrational effects are not taken into account. In short, changing the temperature from 300K to 0K increases the transition pressure by few 0.1 GPa both in experiment and calculation, and neglecting vibrational effects increases the transition pressure by about 1 GPa. On the other hand, Ono *et al.* deduced the relation P=16.7(±0.5)-0.0021(±0.0015)(T-1000) as the experimental phase boundary between α-PbO_2-type and modified fluorite-type structures in SnO_2 [166]. Simple extrapolation yields P=14.6 GPa and 15.2 GPa at 0 K and 300K, respectively. In summary, the difference in transition pressure between 0 K and 300 K is about few 0.1 GPa, and including vibrational effects may result in a change in transition pressure of ~1 GPa.

Turning to the results of our calculations, the effect of U on the transition pressure of ZnO is very small. PBE and PBE+U values, 11.7 and 11.9 GPa, respectively, are too large compared with the upper bound of the experimental values of ~ 9 GPa even when we take vibrational effects into account that would reduce the computational transition pressure by ~1 GPa. On the other hand, the lower bound of the experimental transition pressure of SnO_2 at 300K is 14.2 GPa, and the 0 K transition pressure is estimated to be lower by ~0.6 GPa. LDA (12.8 GPa) therefore appears to underestimate the transition pressure of SnO_2. In summary, PBED3, PBEsol (also PBED3+U and PBEsol+U for ZnO), and SCAN give reasonable transition pressures in both cases.

IV. CONCLUSIONS

This study compared performance of seven approximations, which are PBE, PBE+U, PBED3, PBED3+U, PBEsol, PBEsol+U, and SCAN, regarding the energetics and crystal structure of elementary substances and binary metal oxides with closed-shell electronic structures. Prototype crystal structures were selected from the ICSD, and cation substitution was employed to make a set of existing and hypothetical oxides. A universally applicable procedure is proposed that uses one index each for lattice and internal coordinate relaxation that quantitatively and automatically evaluates the extent of relaxation. PBE and PBE+U show relatively large deformation during relaxation from the experimental structure, and the relaxation is relatively anisotropic in low-dimensional structures. On the other hand, the internal coordinates of SCAN are the

closest to the experimentally reported values.

PBED3, PBEsol, and SCAN reproduced experimental lattice parameters of elementary substances and oxides well with few outliers. Notably, PBEsol and SCAN are found to predict the lattice parameters of low dimensional structures comparably well with PBED3, even though these functionals do not explicitly treat van der Waals interactions. SCAN reproduces the formation enthalpy and Gibbs free energy well, with ME of 0.01 and -0.04 eV, respectively, and RMSE is 0.07 eV in both formation enthalpy and Gibbs free energy. In contrast, all GGAs and those with Hubbard *U* and van der Waals corrections give 0.1 to 0.2 eV ME and at least 0.11 eV RMSE in the formation enthalpy and Gibbs free energy. Phonon calculations for selected systems indicate that the vibrational contribution from solid phases to the enthalpy and Gibbs formation energy is small at less than ~0.1 eV/atom.

The same crystal structure appears as the lowest energy polymorph with different approximations in most of the investigated binary oxides. However, there are some systems where the choice of approximation significantly affects energy differences between polymorphs, or even the order of stability between phases. The energy differences between 201 NaCl and 202 Wurtzite-ZnS(2H) prototypes in ZnO and CdO are reasonable with PBED3, PBED3+*U*, PBEsol, PBEsol+*U*, and SCAN but not with PBE and PBE+*U*. Applying *U* corrections give the rutile structure in TiO_2, which is the easiest to obtain experimentally, as the lowest energy prototype. However, reported quantum Monte Carlo studies suggest that anatase should actually be the ground state [128,141]; the anatase phase is the ground state in PBE, PBEsol, and SCAN. Only PBE, PBE+*U*, and SCAN give the correct stability order of polymorphs derived when anatase TiO_2 is pressurized (anatase to TiO_2-II then TiO_2-III), but PBE and PBE+*U* give as-yet-unreported polymorphs of Nb_2O_5 and Ta_2O_5 as the lowest energy structure, respectively. No approximation gives α-MoO_3, which is the experimentally stable polymorph, as the calculated lowest energy polymorph. PBED3 and PBED3+*U* indicate that the high temperature β-WO_3 phase is stable by ~20 meV/atom compared to low temperature ε-, δ-, and γ-WO_3 phases, but these four polymorphs are almost degenerate in the other approximations. These observations suggest that SCAN is the most reasonable regarding relative energies between polymorphs. The calculated transition

pressure between polymorphs of ZnO and SnO_2 is closest to experimental values when PBED3, PBEsol (also PBED3+*U* and PBEsol+*U* for ZnO), and SCAN are employed, even when zero-point energy contribution and temperature dependence of the transition pressure are considered.

In summary, SCAN appears to be the best choice among the seven approximations based on the analysis of the energetics and crystal structure of binary metal oxides, while PBEsol is the best among the GGAs considered, and shows a comparably good performance with SCAN for many cases. The use of PBEsol+*U* along with PBEsol would also be a reasonable choice as applying +*U* corrections dramatically improve the description of the electronic structure for materials with localized states.

ACKNOWLEDGMENTS

We thank Tomoyasu Yokoyama for helpful discussions. This work was supported by a Grant-in-Aid for Scientific Research on Innovative Areas (Grant No. 25106005) from JSPS, the MEXT Elements Strategy Initiative to Form Core Research Center, Collaborative Research Project of Laboratory for Materials and Structures, as well as PRESTO and the "Materials research by Information Integration" Initiative (MI^2I) project of the Support Program for Starting Up Innovation Hub from Japan Science and Technology Agency (JST). Computing resources of ACCMS at Kyoto University and the Supercomputer Center in the Institute for Solid State Physics at the University of Tokyo were used. The VESTA code [168] was used to draw Figs. 1, 2, 3, and 10.

References

See Supplemental Material at [*URL will be inserted by publisher*] for Supplementary Tables I-LXXIII.

[1] Y.-m. Chiang, D. P. Birnie, and W. D. Kingery, *Physical ceramics : principles for ceramic science and engineering* (J. Wiley, New York, 1997), MIT series in materials science and engineering.

[2] C. N. R. Rao and B. Raveau, *Transition metal oxides : structure, properties, and synthesis of ceramic oxides* (Wiley, New York, 1998).

[3] P. A. Cox, *Transition metal oxides : an introduction to their electronic structure and properties* (Clarendon Press, Oxford, 1992), International series of monographs on chemistry 27.

[4] V. E. Henrich and P. A. Cox, *The surface science of metal oxides* (Cambridge University Press, Cambridge, 1996).

[5] H. Hosono, K. Hayashi, T. Kamiya, T. Atou, and T. Susaki, Sci. Technol. Adv. Mater. **12**, 034303 (2011).

[6] E. Fortunato, P. Barquinha, and R. Martins, Adv. Mater. **24**, 2945 (2012).

[7] M. Lorenz *et al.*, J. Phys. D: Appl. Phys. **49**, 433001 (2016).

[8] S. D. Ha and S. Ramanathan, J. Appl. Phys. **110**, 071101 (2011).

[9] N. K. Elumalai, C. Vijila, R. Jose, A. Uddin, and S. Ramakrishna, Mater. Renew. Sustain. Energy **4**, 11 (2015).

[10] J. C. Védrine and I. Fechete, C. R. Chim. **19**, 1203 (2016).

[11] ICSD database, https://icsd.fiz-karlsruhe.de/search/.

[12] P. Hohenberg and W. Kohn, Phys. Rev. **136**, B864 (1964).

[13] W. Kohn and L. J. Sham, Phys. Rev. **140**, A1133 (1965).

[14] A. Jain *et al.*, APL Mater. **1**, 011002 (2013).

[15] S. Curtarolo *et al.*, Comp. Mater. Sci. **58**, 227 (2012).

[16] S. Kirklin, J. E. Saal, B. Meredig, A. Thompson, J. W. Doak, M. Aykol, S. Rühl, and C. Wolverton, NPJ Comput. Mater. **1**, 15010 (2015).

[17] G. Pizzi, A. Cepellotti, R. Sabatini, N. Marzari, and B. Kozinsky, Comp. Mater. Sci. **111**, 218 (2016).

[18] NOMAD Repository, https://repository.nomad-coe.eu/.

[19] S. P. Ong *et al.*, Comp. Mater. Sci. **68**, 314 (2013).

[20] S. P. Ong, S. Cholia, A. Jain, M. Brafman, D. Gunter, G. Ceder, and K. A. Persson, Comp. Mater. Sci. **97**, 209 (2015).

[21] R. H. Taylor, F. Rose, C. Toher, O. Levy, K. Yang, M. Buongiorno Nardelli, and S. Curtarolo, Comp. Mater. Sci. **93**, 178 (2014).

[22] Y. Kumagai and F. Oba, Phys. Rev. B **89**, 195205 (2014).

[23] Y. Hinuma, G. Pizzi, Y. Kumagai, F. Oba, and I. Tanaka, Comp. Mater. Sci. **128**, 140 (2017).

[24] Y. Hinuma, Y. Kumagai, F. Oba, and I. Tanaka, Comp. Mater. Sci. **113**, 221 (2016).

[25] J. E. Saal, S. Kirklin, M. Aykol, B. Meredig, and C. Wolverton, JOM **65**, 1501 (2013).

[26] S. Curtarolo, G. L. W. Hart, M. B. Nardelli, N. Mingo, S. Sanvito, and O. Levy, Nat. Mater. **12**, 191 (2013).

[27] A. Zakutayev, X. Zhang, A. Nagaraja, L. Yu, S. Lany, T. O. Mason, D. S. Ginley, and A. Zunger, J. Am. Chem. Soc. **135**, 10048 (2013).

[28] Y. Wu, P. Lazic, G. Hautier, K. Persson, and G. Ceder, Energy Environ. Sci. **6**, 157 (2013).

[29] R. Gautier, X. Zhang, L. Hu, L. Yu, Y. Lin, O. L. SundeTor, D. Chon, K. R. Poeppelmeier, and A. Zunger, Nat. Chem. **7**, 308 (2015).

[30] W. Chen *et al.*, J. Mater. Chem. C **4**, 4414 (2016).

[31] Y. Hinuma *et al.*, Nat. Commun. **7**, 11962 (2016).

[32] K. T. Butler, J. M. Frost, J. M. Skelton, K. L. Svane, and A. Walsh, Chem. Soc. Rev. **45**, 6138 (2016).

[33] A. Jain, G. Hautier, S. P. Ong, and K. Persson, J. Mater. Res. **31**, 977 (2016).

[34] W. Sun, S. T. Dacek, S. P. Ong, G. Hautier, A. Jain, W. D. Richards, A. C. Gamst, K. A. Persson, and G. Ceder, Sci. Adv. **2**, e1600225 (2016).

[35] L. Ward, A. Agrawal, A. Choudhary, and C. Wolverton, NPJ Comput. Mater. **2**, 16028 (2016).

[36] J. Lee, A. Seko, K. Shitara, K. Nakayama, and I. Tanaka, Phys. Rev. B **93**, 115104 (2016).

[37] G. Hautier, A. Miglio, G. Ceder, G.-M. Rignanese, and X. Gonze, Nat. Commun. **4**, 2292 (2013).

[38] N. Sarmadian, R. Saniz, B. Partoens, D. Lamoen, K. Volety, G. Huyberechts, and J. Paul, PCCP **16**, 17724 (2014).

[39] I. E. Castelli, T. Olsen, S. Datta, D. D. Landis, S. Dahl, K. S. Thygesen, and K. W. Jacobsen, Energy Environ. Sci. **5**, 5814 (2012).

[40] A. A. Emery, J. E. Saal, S. Kirklin, V. I. Hegde, and C. Wolverton, Chem. Mater. **28**, 5621 (2016).

[41] H. Hayashi, S. Katayama, T. Komura, Y. Hinuma, T. Yokoyama, K. Mibu, F. Oba, and I. Tanaka, Adv. Sci., 1600246 (2016).

[42] K. Yim, Y. Yong, J. Lee, K. Lee, H.-H. Nahm, J. Yoo, C. Lee, C. Seong Hwang, and S. Han, NPG Asia Mater. **7**, e190 (2015).

[43] I. E. Castelli *et al.*, Advanced Energy Materials **5**, 1400915 (2015).

[44] A. E. Mattsson, Science **298**, 759 (2002).

[45] J. P. Perdew and Y. Wang, Phys. Rev. B **33**, 8800 (1986).

[46] J. Tao, J. P. Perdew, V. N. Staroverov, and G. E. Scuseria, Phys. Rev. Lett. **91**, 146401 (2003).

[47] J. Sun *et al.*, Nat Chem **8**, 831 (2016).

[48] J. Sun, A. Ruzsinszky, and J. P. Perdew, Phys. Rev. Lett. **115**, 036402 (2015).

[49] V. I. Anisimov, J. Zaanen, and O. K. Andersen, Phys. Rev. B **44**, 943 (1991).

[50] S. L. Dudarev, G. A. Botton, S. Y. Savrasov, C. J. Humphreys, and A. P. Sutton, Phys. Rev. B **57**, 1505 (1998).

[51] A. D. Becke and E. R. Johnson, J. Chem. Phys. **122**, 154104 (2005).

[52] A. Tkatchenko and M. Scheffler, Phys. Rev. Lett. **102**, 073005 (2009).

[53] S. Grimme, J. Antony, S. Ehrlich, and H. Krieg, J. Chem. Phys. **132**, 154104 (2010).

[54] H. Peng, Z.-H. Yang, J. P. Perdew, and J. Sun, Physical Review X **6**, 041005 (2016).

[55] A. D. Becke, J. Chem. Phys. **98**, 5648 (1993).

[56] J. Perdew, M. Ernzerhof, and K. Burke, J. Chem. Phys. **105**, 9982 (1996).

[57] C. Adamo and V. Barone, J. Chem. Phys. **110**, 6158 (1999).

[58] M. Ernzerhof and G. Scuseria, J. Chem. Phys. **110**, 5029 (1999).

[59] J. Heyd, G. Scuseria, and M. Ernzerhof, J. Chem. Phys. **118**, 8207 (2003).

[60] D. M. Bylander and L. Kleinman, Phys. Rev. B **41**, 7868 (1990).

[61] R. Asahi, W. Mannstadt, and A. J. Freeman, Phys. Rev. B **59**, 7486 (1999).

[62] A. V. Krukau, O. A. Vydrov, A. F. Izmaylov, and G. E. Scuseria, J. Chem. Phys. **125**, 224106 (2006).

[63] J. Paier, M. Marsman, K. Hummer, G. Kresse, I. C. Gerber, and J. G. Angyan, J. Chem. Phys. **124**, 154709 (2006).

[64] S. J. Clark and J. Robertson, Phys. Rev. B **82**, 085208 (2010).

[65] A. Grüneis, G. Kresse, Y. Hinuma, and F. Oba, Phys. Rev. Lett. **112**, 096401 (2014).

[66] Y. Hinuma, A. Grüneis, G. Kresse, and F. Oba, Phys. Rev. B **90**, 155405 (2014).

[67] F. Oba, M. Choi, A. Togo, and I. Tanaka, Sci. Technol. Adv. Mater. **12**, 034302 (2011).

[68] D. C. Langreth and J. P. Perdew, Phys. Rev. B **15**, 2884 (1977).

[69] L. Hedin, Phys. Rev. **139**, A796 (1965).

[70] W. M. C. Foulkes, L. Mitas, R. J. Needs, and G. Rajagopal, Rev. Mod. Phys. **73**, 33 (2001).

[71] G. H. Booth, A. Gruneis, G. Kresse, and A. Alavi, Nature **493**, 365 (2013).

[72] F. Tran, Phys. Lett. A **376**, 879 (2012).

[73] Y. Hinuma, Y. Kumagai, I. Tanaka, and F. Oba, Phys. Rev. B **95**, 075302 (2017).

[74] G. I. Csonka, J. P. Perdew, A. Ruzsinszky, P. H. T. Philipsen, S. Lebègue, J. Paier, O. A. Vydrov, and J. G. Ángyán, Phys. Rev. B **79**, 155107 (2009).

[75] P. Haas, F. Tran, and P. Blaha, Phys. Rev. B **79**, 085104 (2009).

[76] L. Goerigk, H. Kruse, and S. Grimme, ChemPhysChem **12**, 3421 (2011).

[77] L. He, F. Liu, G. Hautier, M. J. T. Oliveira, M. A. L. Marques, F. D. Vila, J. J. Rehr, G. M. Rignanese, and A. Zhou, Phys. Rev. B **89**, 064305 (2014).

[78] J. P. Perdew, K. Burke, and M. Ernzerhof, Phys. Rev. Lett. **77**, 3865 (1996).

[79] J. P. Perdew, A. Ruzsinszky, G. I. Csonka, O. A. Vydrov, G. E. Scuseria, L. A. Constantin, X. Zhou, and K. Burke, Phys. Rev. Lett. **100**, 136406 (2008).

[80] I. V. Solovyev, P. H. Dederichs, and V. I. Anisimov, Phys. Rev. B **50**, 16861 (1994).

[81] A. Janotti, D. Segev, and C. G. Van de Walle, Phys. Rev. B **74**, 045202 (2006).

[82] M. Choi, F. Oba, and I. Tanaka, Phys. Rev. Lett. **103**, 185502 (2009).

[83] M. Choi, F. Oba, Y. Kumagai, and I. Tanaka, Adv. Mater. **25**, 86 (2013).

[84] P. E. Blöchl, Phys. Rev. B **50**, 17953 (1994).

[85] G. Kresse and J. Furthmüller, Phys. Rev. B **54**, 11169 (1996).

[86] G. Kresse and D. Joubert, Phys. Rev. B **59**, 1758 (1999).

[87] V. Stevanović, S. Lany, X. Zhang, and A. Zunger, Phys. Rev. B **85**, 115104 (2012).

[88] F. Zhou, M. Cococcioni, C. A. Marianetti, D. Morgan, and G. Ceder, Phys. Rev. B **70**, 235121 (2004).

[89] N. J. Mosey, P. Liao, and E. A. Carter, J. Chem. Phys. **129**, 014103 (2008).

[90] A. Togo and I. Tanaka, Scripta Mater. **108**, 1 (2015).

[91] M. W. Chase, Jr., *NIST-JANAF thermochemical tables* (American Chemical Society and American Institute of Physics for the National Institute of Standards and Technology, New York : Washington, D.C., 1998), Fourth edn.

[92] J. D. Cox, D. D. Wagman, and V. A. Medvedev, *CODATA key values for thermodynamics* (Hemisphere Pub. Corp., New York, 1984).

[93] M. Binnewies and E. Milke, *Thermochemical data of elements and compounds* (Wiley-VCH, Weinheim, 2002).

[94] D. R. Lide, *CRC handbook of chemistry and physics : a ready-reference book of chemical and physical data* (CRC Press, Boca Raton, FL, 1998).

[95] L. Wang, T. Maxisch, and G. Ceder, Phys. Rev. B **73**, 195107 (2006).

[96] N. Weiher, E. A. Willneff, C. Figulla-Kroschel, M. Jansen, and S. L. M. Schroeder, Solid State Commun. **125**, 317 (2003).

[97] H. Sabrowsky, Z. Anorg. Allg. Chem. **381**, 266 (1971).

[98] Y. Chen *et al.*, Appl. Phys. Lett. **108**, 152105 (2016).

[99] J.-M. Raulot, G. Baldinozzi, R. Seshadri, and P. Cortona, Solid State Sci. **4**, 467 (2002).

[100] R. Shannon, Acta Crystallographica Section A **32**, 751 (1976).

[101] M. Moses-DeBusk, M. Yoon, L. F. Allard, D. R. Mullins, Z. Wu, X. Yang, G. Veith, G. M. Stocks, and C. K. Narula, J. Am. Chem. Soc. **135**, 12634 (2013).

[102] C. K. Narula, L. F. Allard, G. M. Stocks, and M. Moses-DeBusk, **4**, 7238 (2014).

[103] R. Roy, V. G. Hill, and E. F. Osborn, J. Am. Chem. Soc. **74**, 719 (1952).

[104] M. Zinkevich and F. Aldinger, J. Am. Ceram. Soc. **87**, 683 (2004).

[105] M. Zinkevich, Prog. Mater Sci. **52**, 597 (2007).

[106] A. Matsumoto, Y. Koyama, A. Togo, M. Choi, and I. Tanaka, Phys. Rev. B **83**, 214110 (2011).

[107] S. Sanna *et al.*, Nat Mater **14**, 500 (2015).

[108] National Research Council (US) Committee on Medical and Biological Effects of Environmental Pollutants, *Arsenic: Medical and Biologic Effects of Environmental Pollutants* (National Academies Press (US), Washington DC, 1977).

[109] A. F. Wells, *Structural Inorganic Chemistry* (Clarendon Press, Oxford, 1984).

[110] A. Matsumoto, Y. Koyama, and I. Tanaka, Phys. Rev. B **81**, 094117 (2010).

[111] V. Swamy, S. K. Saxena, B. Sundman, and J. Zhang, J. Geophys. Res. Solid Earth **99**, 11787 (1994).

[112] F. J. Bates, F. P. Phelps, and S. United, *A suggested new base point on the thermometric scale and the α-β inversion of quartz* (U.S. Dept. of Commerce, Bureau of Standards : U.S. Govt. Print. Off., Washington, D.C., 1927), Scientific Papers of the Bureau of Standards ;no. 557, p. 315-327.

[113] A. B. Thompson and M. Wennemer, Am. Mineral. **64**, 1018 (1979).

[114] V. Dmitriev, V. Torgashev, P. Tolédano, and E. K. H. Salje, Europhys. Lett. **37**, 553 (1997).

[115] V. P. Prakapenka, G. Shen, L. S. Dubrovinsky, M. L. Rivers, and S. R. Sutton, J. Phys. Chem. Solids **65**, 1537 (2004).

[116] T. Kubo, T. Kato, Y. Higo, and K.-i. Funakoshi, Sci. Adv. **1**, e1500075 (2015).

[117] J. Shropshire, P. Keat Paul, and A. Vaughan Philip, Z. Kristallogr. Cryst. Mater. **112**, 409 (1959).

[118] P. J. Heaney and J. E. Post, Am. Mineral. **86**, 1358 (2001).

[119] R. A. Robie, B. S. Hemingway, and J. R. Fisher, *Thermodynamic properties of minerals and related substances at 298.15 K and 1 bar (105 pascals) pressure and at higher temperatures* (U.S. Geological Survey, Washington DC, 1978).

[120] J. L. Holm, O. J. Kleppa, and E. F. Westrum Jr, Geochim. Cosmochim. Acta **31**, 2289 (1967).

[121] I. Petrovic, P. J. Heaney, and A. Navrotsky, Phys. Chem. Miner. **23**, 119 (1996).

[122] S. Ono, T. Tsuchiya, K. Hirose, and Y. Ohishi, Phys. Rev. B **68**, 014103 (2003).

[123] J. Haines and J. M. Léger, Phys. Rev. B **55**, 11144 (1997).

[124] S. Ono, E. Ito, T. Katsura, A. Yoneda, M. J. Walter, S. Urakawa, W. Utsumi, and K. Funakoshi, Phys. Chem. Miner. **27**, 618 (2000).

[125] J. P. Carr and N. A. Hampson, Chem. Rev. **72**, 679 (1972).

[126] J. Haines, J. M. Léger, and O. Schulte, J. Phys.: Condens. Matter **8**, 1631 (1996).

[127] B. Grocholski, S.-H. Shim, E. Cottrell, and V. B. Prakapenka, Am. Mineral. **99**, 170 (2014).

[128] L. Ye, B. Anouar, S. Luke, T. K. Jaron, H. Olle, and R. C. K. Paul, New J. Phys. **18**, 113049 (2016).

[129] H. Kazuhito, I. Hiroshi, and F. Akira, Jpn. J. Appl. Phys. **44**, 8269 (2005).

[130] A. Di Paola, M. Bellardita, and L. Palmisano, Catalysts **3**, 36 (2013).

[131] M. R. Ranade *et al.*, Proc. Natl. Acad. Sci. USA **99**, 6476 (2002).

[132] D. A. H. Hanaor and C. C. Sorrell, J. Mater. Sci. **46**, 855 (2011).

[133] S. J. Smith, R. Stevens, S. Liu, G. Li, A. Navrotsky, J. Boerio-Goates, and B. F. Woodfield, Am. Mineral. **94**, 236 (2009).

[134] T. Arlt, M. Bermejo, M. A. Blanco, L. Gerward, J. Z. Jiang, J. S. Olsen, and J. M. Recio, Phys. Rev. B **61**, 14414 (2000).

[135] T. Sekiya, S. Ohta, S. Kamei, M. Hanakawa, and S. Kurita, J. Phys. Chem. Solids **62**, 717 (2001).

[136] K. Lagarec and S. Desgreniers, Solid State Commun. **94**, 519 (1995).

[137] J. Akimoto, Y. Gotoh, Y. Oosawa, N. Nonose, T. Kumagai, K. Aoki, and H. Takei, J. Solid State Chem. **113**, 27 (1994).

[138] T. P. Feist and P. K. Davies, J. Solid State Chem. **101**, 275 (1992).

[139] M. Latroche, L. Brohan, R. Marchand, and M. Tournoux, J. Solid State Chem. **81**, 78 (1989).

[140] M. T. Curnan and J. R. Kitchin, J. Phys. Chem. C **119**, 21060 (2015).

[141] J. Trail, B. Monserrat, P. López Ríos, R. Maezono, and R. J. Needs, Phys. Rev. B **95**, 121108 (2017).

[142] B. Monserrat, N. D. Drummond, and R. J. Needs, Phys. Rev. B **87**, 144302 (2013).

[143] A. Jayaraman, S. Y. Wang, S. K. Sharma, and L. C. Ming, Phys. Rev. B **48**, 9205 (1993).

[144] O. Ohtaka, H. Fukui, T. Kunisada, T. Fujisawa, K. Funakoshi, W. Utsumi, T. Irifune, K. Kuroda, and T. Kikegawa, J. Am. Ceram. Soc. **84**, 1369 (2001).

[145] Y. Al-Khatatbeh and K. K. M. Lee, J. Superhard Mater. **36**, 231 (2014).

[146] J. M. Leger, P. E. Tomaszewski, A. Atouf, and A. S. Pereira, Phys. Rev. B **47**, 14075 (1993).

[147] E. H. Kisi, C. J. Howard, and R. J. Hill, J. Am. Ceram. Soc. **72**, 1757 (1989).

[148] P. Balog, D. Orosel, Z. Cancarevic, C. Schön, and M. Jansen, J. Alloys Compd. **429**, 87 (2007).

[149] J. M. Cocciantelli, P. Gravereau, J. P. Doumerc, M. Pouchard, and P. Hagenmuller, J. Solid State Chem. **93**, 497 (1991).

[150] J. B. Goodenough, A. Hamnett, G. Huber, F. Hullinger, M. Leiß, S. K. Ramasesha, and H. Werheit, *Physics of Non-Tetrahedrally Bonded Binary Compounds III / Physik der nicht-tetraedrisch gebundenen binären Verbindungen III* (Springer-Verlag Berlin Heidelberg, Berlin, 1984), Vol. 17g.

[151] H. Kodama, T. Kikuchi, and M. Goto, J. Less Common Met. **29**, 415 (1972).

[152] S. Tamura, J. Mater. Sci. **7**, 298 (1972).

[153] K. Kato, Acta Cryst. B **32**, 764 (1976).

[154] C. Askeljung, B.-O. Marinder, and M. Sundberg, J. Solid State Chem. **176**, 250 (2003).

[155] I. P. Zibrov, V. P. Filonenko, M. Sundberg, and P.-E. Werner, Acta Cryst. B **56**, 659 (2000).

[156] E. M. McCarron and J. C. Calabrese, J. Solid State Chem. **91**, 121 (1991).

[157] E. Cazzanelli, C. Vinegoni, G. Mariotto, A. Kuzmin, and J. Purans, Solid State Ion. **123**, 67 (1999).

[158] A. D. Walkingshaw, N. A. Spaldin, and E. Artacho, Phys. Rev. B **70**, 165110 (2004).

[159] A. Werner and H. D. Hochheimer, Phys. Rev. B **25**, 5929 (1982).

[160] C. H. Bates, W. B. White, and R. Roy, Science **137**, 993 (1962).

[161] S. Desgreniers, Phys. Rev. B **58**, 14102 (1998).

[162] H. Karzel *et al.*, Phys. Rev. B **53**, 11425 (1996).

[163] J. M. Recio, M. A. Blanco, V. Luaña, R. Pandey, L. Gerward, and J. S. Olsen, Phys. Rev. B **58**, 8949 (1998).

[164] K. Kusaba, Y. Syono, and T. Kikegawa, Proceedings of the Japan Academy, Series B **75**, 1 (1999).

[165] K. Inoue, University of Tokyo, 1975.

[166] S. Ono, K. Funakoshi, A. Nozawa, and T. Kikegawa, J. Appl. Phys. **97**, 073523 (2005).

[167] A. Seko, F. Oba, A. Kuwabara, and I. Tanaka, Phys. Rev. B **72**, 024107 (2005).

[168] K. Momma and F. Izumi, J. Appl. Crystallogr. **44**, 1272 (2011).

[169] Z. Shao-Min, G. He-Chun, Z. Bin, D. Zu-Liang, Z. Xing-Tang, and W. Si-Xin, Nanotechnology **19**, 175303 (2008).

Table I. List of prototype structures selected from the ICSD. The structure type in ICSD is used as the prototype name unless shown otherwise. Internal coordinates for TiO_2 in the Baddeleyite-ZrO_2(*mP*12) structure type differs significantly from HfO_2, thus is considered a separate prototype from the latter.

Prototype ID	ICSD Coll code	Space group type	Space group number	Z	ICSD structure type	Notes
101	20368	$P\bar{3}m$	164	1	Ag_2F	Prototype name: Anti-CdI_2
102	27919	$R\bar{3}m$	166	3	$CdCl_2$ (3R)	Prototype name: Anti-$CdCl_2$(3R)
103	77676	$Fm\bar{3}m$	225	4	Fluorite-CaF_2	Prototype name: Anti-Fluorite-CaF_2
104	261853	$Pn\bar{3}m$	224	2	Cu_2O	Cuprite structure
201	163628	$Fm\bar{3}m$	255	4	NaCl	Rocksalt structure
202	162843	$P6_3mc$	186	2	Wurtzite-ZnS (2H)	
203	29082	$F\bar{4}3m$	216	4	Sphalerite-ZnS (*cF*8)	Zincblende structure
204	18147	$P4_2/mnm$	136	4	BeO (*tP*8)	
205	40316	*Pnma*	62	4	HgO	Montroydite HgO
206	639125	$P3_121$	152	3	HgS	Cinnabar HgO
207	15402	*Pbcm*	57	4	Massicot	
208	62842	*P*4/*nmm*	129	2	Litharge	
209	173921	$P6_3/mmc$	194	2	Nickeline-NiAs	
301	169172	$Ia\bar{3}$	206	16	Bixbyite-Mn_2O_3	δ-Ga_2O_3 C-type rare earth sesquioxide
302	75560	$R\bar{3}c$	167	6	Corundum-Al_2O_3	α-Al_2O_3 α-Ga_2O_3
303	192270	$P\bar{3}m1$	164	1	La_2O_3	A-type rare earth sesquioxide
304	83645	*C*2/*m*	12	4	Ga_2O_3	θ-Al_2O_3 β-Ga_2O_3
305	16021	$P3_1$	144	3	B_2O_3	
306	238641	$P2_1/n$	14	4	As_2O_3	Claudetite As_2O_3
307	238612	$Fd\bar{3}m$	227	16	As_2O_3 (*cF*80)	Arsenolite As_2O_3 α-Sb_2O_3
308	240207	*Pccn*	56	4	Sb_2O_3	β-Sb_2O_3 ε-Bi_2O_3
309	168567	$P2_1/c$	14	4	Bi_2O_3	α-Bi_2O_3
310	189995	$P\bar{4}2_1c$	114	4	Bi_2O_3 (*tP*20)	β-Bi_2O_3
401	39166	$P4_2/mnm$	136	2	Rutile-TiO_2	Stishovite SiO_2

402	9852	$I4_1/amd$	141	4	Anatase-TiO_2	β-PbO_2
403	36408	*Pbca*	61	8	Brookite-TiO_2	Prototype name: Brookite-TiO_2 (TiO_2)
404	79913	*Pbca*	61	8	Brookite-TiO_2	Prototype name: Brookite-TiO_2 (HfO_2)
405	94887	$P2_1/c$	14	4	Baddeleyite-ZrO_2 (*mP*12)	TiO_2-III
406	415269	*Pbcn*	60	4	PbO_2-alpha	Seifertite SiO_2 TiO_2-II
407	75179	*Pnma*	62	4	VO_2	TiO_2 (R)
408	41056	*C*2/*m*	12	8	VO_2 (HT)	TiO_2 (B)
409	67004	$Pca2_1$	29	4	ZrO_2 (*oP*12)	
410	173966	$P4_2/nmc$	137	2	Zirconia-ZrO_2 (HT)	
411	173967	$Fm\bar{3}m$	225	4	Fluorite-CaF_2	Yttrium stabilized zirconia structure
412	83863	*Pnma*	62	4	HfO_2	Cottunite-type PbO_2
413	281599	*Pnnm*	58	2	$CaCl_2$	Rutile with lowered symmetry
414	281601	$Pa\bar{3}$	205	4	PdF_2 (*cP*12)	"Pyrite-type" "Modified fluorite-type"
415	62405	$P3_221$	154	3	Quartz,low	α-quartz SiO_2
416	67669	*C*2/*c*	15	12	Moganite	α-moganite SiO_2
417	77452	$P4_12_12$	92	4	Cristobalite (alpha)	α-cristobalite SiO_2
418	172286	*C*2/*c*	4	16	Coesite	Coesite SiO_2
501	60767	*Pmmn*	59	2	V_2O_5	α-V_2O_5
502	59961	$P2_1/m$	11	2	V_2O_5 ($P2_1/m$)	β-V_2O_5 δ-V_2O_5
503	71317	*C*2/*c*	15	4	Sb_2O_5	B-(ζ-)Nb_2O_5 B-Ta_2O_5
601	16031	*Ama*2	40	4	CrO_3	
602	151751	*Pnma*	62	1	MoO_3	α-MoO_3
603	84168	*Pc*	7	3	WO_3 (*mP*16)	ε-WO_3
604	80053	$P\bar{1}$	2	4	WO_3 (*aP*32)	δ-WO_3
605	16080	$P2_1/n$	14	2	WO_3 (*mP*32)	γ-WO_3 β'-MoO_3
606	50728	*Pcnb*	60	4	WO_3 (HT)	β-WO_3
607	108651	$Pm\bar{3}m$	221	2	ReO_3	Tungsten bronze framework

Table II. Cation species considered in this study.

Valence	Elements
+1	Li, Na, K, Rb, Cs, Cu, Ag, Au, Tl
+2	Be, Mg, Ca, Sr, Ba, Zn, Cd, Hg, Sn, Pb
+3	Sc, Y, La, Al, Ga, In, B, As, Sb, Bi
+4	Ti, Zr, Hf, Si, Ge, Sn, Pb
+5	V, Nb, Ta
+6	Cr, Mo, W

Table III. Mean error (ME), mean absolute error (MAE), and root mean square error (RMSE) of lattice parameters of elementary substances. Data are given for 3D structures (3D) as well as lattice parameters of low-dimensional structures in axes with (LD-s) and without (LD-nos) spacing between atoms. Individual errors are given in Supplementary Tables II-VIII. (+*U*) values are not given for LD structures as U_{eff}=0 for all LD systems.

	ME			MAE			RMSE		
	3D	LD-s	LD-nos	3D	LD-s	LD-nos	3D	LD-s	LD-nos
PBE	0.2%	8.0%	1.1%	1.5%	9.0%	1.2%	3.2%	10.7%	1.3%
PBE(+*U*)	1.2%			2.2%			4.1%		
PBED3	-1.4%	-2.2%	-0.2%	1.7%	2.9%	0.8%	2.1%	2.9%	1.5%
PBED3(+*U*)	-0.5%			2.3%			3.5%		
PBEsol	-1.4%	-1.6%	-0.2%	1.7%	3.3%	0.7%	2.2%	4.2%	1.2%
PBEsol(+*U*)	-0.5%			2.0%			3.1%		
SCAN	-0.7%	0.5%	0.3%	1.5%	2.1%	0.8%	2.7%	3.3%	1.2%

Table IV. Largest positive and negative errors in lattice parameters of elementary substances. Data are given for 3D structures (3D) as well as lattice parameters of low-dimensional structures in axes with (LD-s) and without (LD-nos) spacing between atoms. Individual errors are given in Supplementary Tables II-VIII. (+*U*) values are not given for LD structures as U_{eff}=0 for all LD systems.

	Largest positive error			Largest negative error		
	3D	LD-s	LD-nos	3D	LD-s	LD-nos
PBE	31.3%	27.8%	4.3%	-8.3%	-8.2%	-0.2%
PBE(+*U*)	31.3%			-9.9%		
PBED3	3.6%	3.8%	0.9%	-10.8%	-10.7%	-4.6%
PBED3(+*U*)	13.4%			-8.3%		
PBEsol	4.9%	6.5%	0.8%	-12.3%	-13.5%	-3.6%
PBEsol(+*U*)	12.9%			-8.6%		
SCAN	14.7%	6.7%	3.4%	-12.6%	-9.4%	-0.7%

Table V. Mean error (ME), mean absolute error (MAE), and root mean square error (RMAE) of lattice parameters of binary oxides. Data are given for 3D structures (3D) as well as lattice parameters of low-dimensional structures in axes with (LD-s) and without (LD-nos) spacing between atoms. Individual errors are given in Supplementary Tables XI-XXIV.

	ME			MAE			RMSE		
	3D	LD-s	LD-ns	3D	LD-s	LD-ns	3D	LD-s	LD-ns
PBE	1.3%	6.2%	2.3%	1.4%	3.4%	4.1%	1.1%	4.6%	2.4%
PBE(+*U*)	1.4%	5.9%	3.0%	1.6%	3.9%	4.7%	1.2%	5.5%	3.4%
PBED3	0.3%	0.2%	0.4%	0.8%	1.1%	0.9%	1.0%	1.8%	0.9%
PBED3(+*U*)	0.4%	0.0%	0.8%	1.0%	1.3%	1.2%	1.2%	2.0%	1.6%
PBEsol	0.0%	0.5%	-0.3%	0.7%	0.7%	1.4%	1.0%	2.8%	1.1%
PBEsol(+*U*)	0.1%	0.4%	0.1%	1.0%	0.9%	1.8%	1.2%	3.0%	1.6%
SCAN	-0.2%	0.5%	0.1%	0.6%	0.7%	1.0%	0.8%	1.4%	1.1%

Table VI. Largest positive and negative errors in lattice parameters of binary oxides. Data are given for 3D structures (3D) as well as lattice parameters of low-dimensional structures in axes with (LD-s) and without (LD-nos) spacing between atoms. Individual errors are given in Supplementary Tables XI-XXIV.

	Largest positive error			Largest negative error		
	3D	LD-s	LD-ns	3D	LD-s	LD-ns
PBE	5.8%	18.3%	9.0%	-4.4%	0.5%	-0.2%
PBE(+*U*)	5.8%	18.3%	11.1%	-4.4%	-8.9%	-0.7%
PBED3	2.8%	5.6%	1.7%	-5.5%	-2.3%	-1.4%
PBED3(+*U*)	3.1%	5.6%	5.0%	-5.5%	-4.8%	-1.4%
PBEsol	3.8%	9.0%	1.0%	-6.3%	-4.0%	-3.1%
PBEsol(+*U*)	3.1%	9.0%	3.5%	-6.3%	-5.2%	-3.1%
SCAN	2.0%	5.2%	2.2%	-6.0%	-2.1%	-1.6%

Table VII. Means of indices of deformation (LR_2, *CR*, *CR*') for 3D and LD structures in various approximations. Individual indices are given in Supplementary Tables XXV-XXVII.

	LR_2		*CR* (Å)		*CR*'	
	3D	LD	3D	LD	3D	LD
PBE	0.000	0.010	0.051	0.101	0.008	0.018
PBE(+*U*)	0.000	0.014	0.052	0.102	0.009	0.018
PBED3	0.000	0.001	0.037	0.051	0.007	0.010
PBED3(+*U*)	0.000	0.002	0.039	0.047	0.007	0.009
PBEsol	0.000	0.003	0.039	0.063	0.007	0.012
PBEsol(+*U*)	0.000	0.003	0.040	0.064	0.007	0.012
SCAN	0.000	0.001	0.030	0.037	0.005	0.007

Table VIII. Vibrational contributions to the formation enthalpy at 298K (ΔH_f^{vib}) and formation Gibbs free energy at 298K (ΔG_f^{vib}) calculated using the PBEsol functional for selected systems. The change in the Gibbs free energy when the vibrational contribution is accounted for in the reference O_2 gas only, $\Delta G_f^{vib,O}$, and ΔG_f^{vib}-$\Delta G_f^{vib,O}$ are also shown. The values are relative to the formation energy at 0K excluding vibrational effects. Units are in eV/atom.

Compound	Prototype	ΔH_f^{vib}	ΔG_f^{vib}	$\Delta G_f^{vib,O}$	ΔG_f^{vib}-$\Delta G_f^{vib,O}$
BeO	202 Wurtzite-ZnS (2H)	0.06	0.22	0.13	0.09
MgO	201 NaCl	-0.04	0.15	0.13	0.02
PbO	208 Litharge	0.03	0.14	0.13	0.01
Al_2O_3	302 Corundum-Al_2O_3	-0.02	0.13	0.16	-0.03
Ga_2O_3	304 Ga_2O_3	-0.01	0.14	0.16	-0.02
In_2O_3	301 Bixbyite-Mn_2O_3	-0.01	0.15	0.16	-0.01
La_2O_3	303 La_2O_3	0.03	0.14	0.16	-0.02
SnO_2	401 Rutile-TiO_2	0.05	0.15	0.18	-0.03
PbO_2	406 PbO_2-alpha	0.05	0.13	0.18	-0.04
TiO_2	402 Anatase-TiO_2	0.05	0.14	0.18	-0.04

Table IX. Mean error (ME), mean absolute error (MAE), and root mean square error (RMAE) of the difference between calculated and experimental formation enthalpy, $\Delta H_{f(calc)}$-$\Delta H_{f(exp)}$, and Gibbs free energy, $\Delta G_{f(calc)}$-$\Delta G_{f(exp)}$, for each approximation. Individual errors in formation enthalpy and Gibbs free energy are given in Supplementary Tables XXIX and XXXI, respectively. Units are in eV/atom.

	$\Delta H_{f(calc)}$-$\Delta H_{f(exp)}$			$\Delta G_{f(calc)}$-$\Delta G_{f(exp)}$		
	ME	MAE	RMSE	ME	MAE	RMSE
PBE	0.24	0.24	0.13	0.19	0.20	0.13
PBE(+*U*)	0.22	0.23	0.13	0.17	0.19	0.12
PBED3	0.18	0.20	0.12	0.14	0.16	0.12
PBED3(+*U*)	0.17	0.18	0.12	0.12	0.14	0.12
PBEsol	0.17	0.18	0.11	0.12	0.14	0.11
PBEsol(+*U*)	0.15	0.16	0.12	0.10	0.13	0.11
SCAN	0.01	0.06	0.07	-0.04	0.06	0.07

Table X. Lattice parameters and internal coordinates of SnO. Units: *a*, *c*, and 2*uc* in angstroms, *c*/*a* and *u* are dimensionless. Experimental data is ICSD coll code 16481.

	a	*c*	*c/a*	*u*	*2uc*
Experiment	3.803	4.838	1.272	0.238	2.306
PBE	3.858	5.027	1.303	0.231	2.320
PBED3	3.824	4.729	1.237	0.246	2.324
PBEsol	3.798	4.723	1.244	0.245	2.310
SCAN	3.794	4.863	1.282	0.237	2.301

Table XI. Lattice parameters and internal coordinates of PbO. Units: *a*, *c*, and 2*uc* in angstroms, *c*/*a* and *u* are dimensionless. Experimental data is ICSD coll code 62842.

	a	*c*	*c/a*	*u*	*2uc*
Experiment	3.974	5.022	1.264	0.235	2.361
PBE	4.050	5.523	1.364	0.215	2.372
PBED3	4.031	4.943	1.226	0.239	2.364
PBEsol	3.988	5.033	1.262	0.235	2.364
SCAN	3.982	5.106	1.282	0.232	2.366

Table XII. Transition pressures for 202 Wurtzite-ZnS (2H) to 201 NaCl rocksalt prototype in ZnO and 406 PbO_2-alpha to 414 PdF_2 (*cP*12) prototype in SnO_2. U_{eff}=0 in SnO_2, hence no values are shown for +*U*.

	ZnO	SnO_2
PBE	11.7	18.2
PBED3	7.9	14.7
PBEsol	8.9	14.5
LDA	9.1	12.8
SCAN	8.0	17.6
PBE+*U*	11.9	
PBED3+*U*	7.6	
PBEsol+*U*	8.6	
LDA+*U*	8.2	
Experiment	6.3 [164] 7.3 [165] 9 [98,160-163]	14.2-21 [123] 15.2 [166]

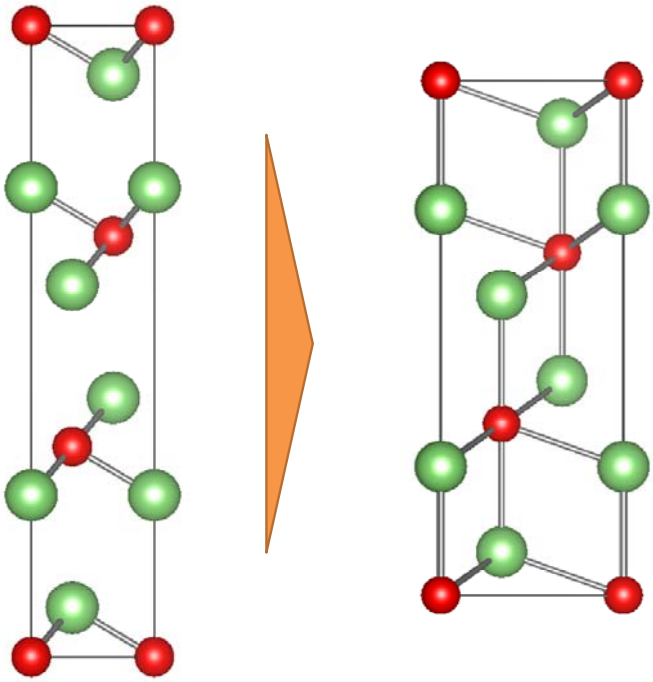

Fig. 1. Relaxation of Li_2O from the 102 Anti-$CdCl_2$(3R) prototype. Green balls: Li, red balls: O.

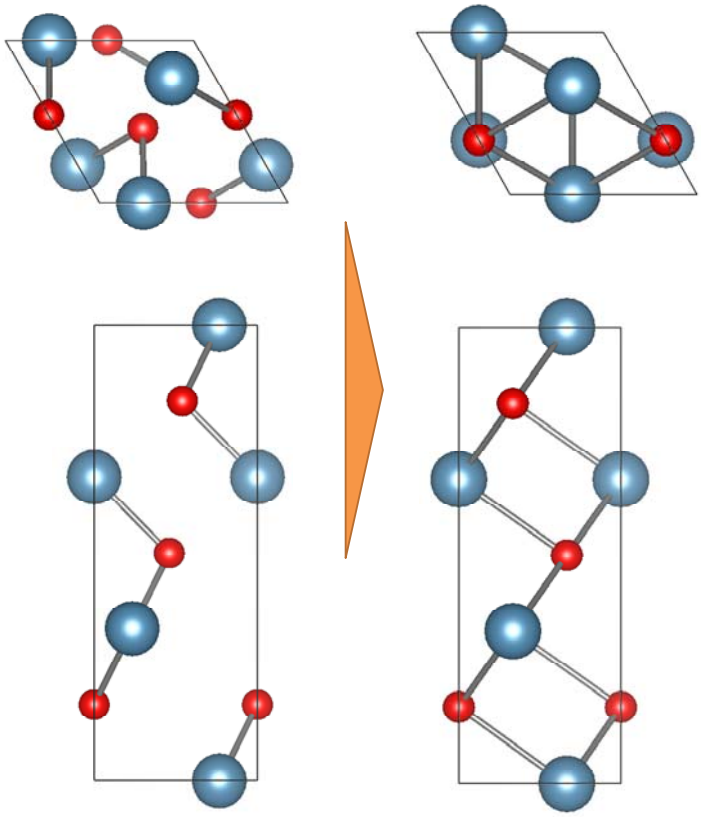

Fig. 2. Relaxation of CaO from the 206 HgS prototype (viewed from two directions). Blue balls: Ca, red balls: O.

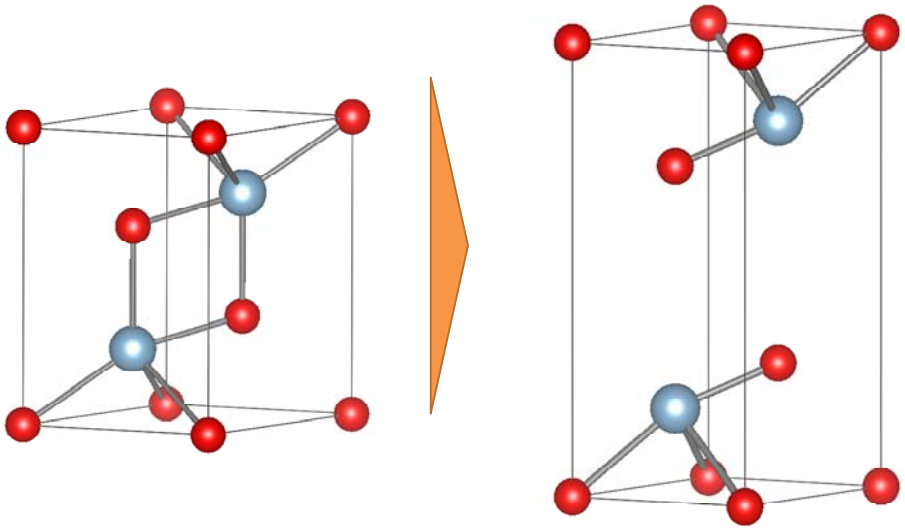

Fig. 3. Relaxation of Al_2O_3 from the 303 La_2O_3 prototype. Blue balls: Al, red balls: O.

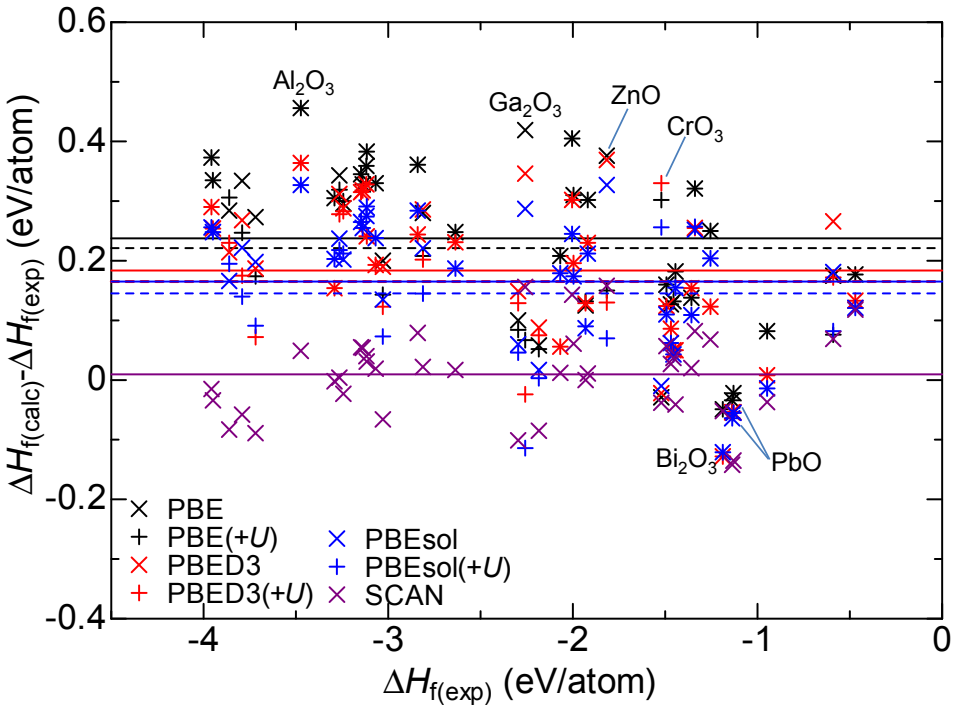

Fig. 4. Experimental formation enthalpy, $\Delta H_{f(exp)}$, versus difference between calculated and experimental formation enthalpy, $\Delta H_{f(calc)}$-$\Delta H_{f(exp)}$. The average of $\Delta H_{f(calc)}$-$\Delta H_{f(exp)}$ over all systems, $<\Delta H_{f(calc)}$-$\Delta H_{f(exp)}>$, for each approximation is shown: solid and broken lines indicate values without and with (+*U*), respectively.

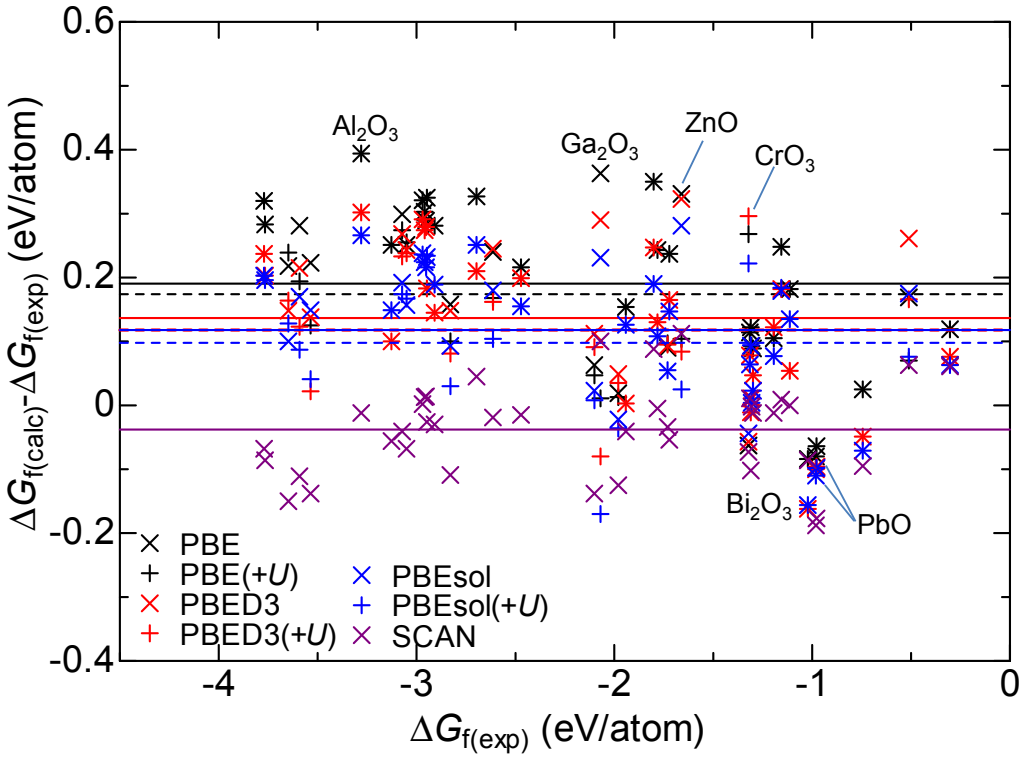

Fig. 5. Experimental formation Gibbs free energy, $\Delta G_{f(exp)}$, versus difference between calculated and experimental formation Gibbs free energy, $\Delta G_{f(calc)}$-$\Delta G_{f(exp)}$. The average of $\Delta G_{f(calc)}$-$\Delta G_{f(exp)}$ over all systems, $\langle \Delta G_{f(calc)}$-$\Delta G_{f(exp)} \rangle$, for each approximation is shown: solid and broken lines indicate values without and with (+*U*), respectively.

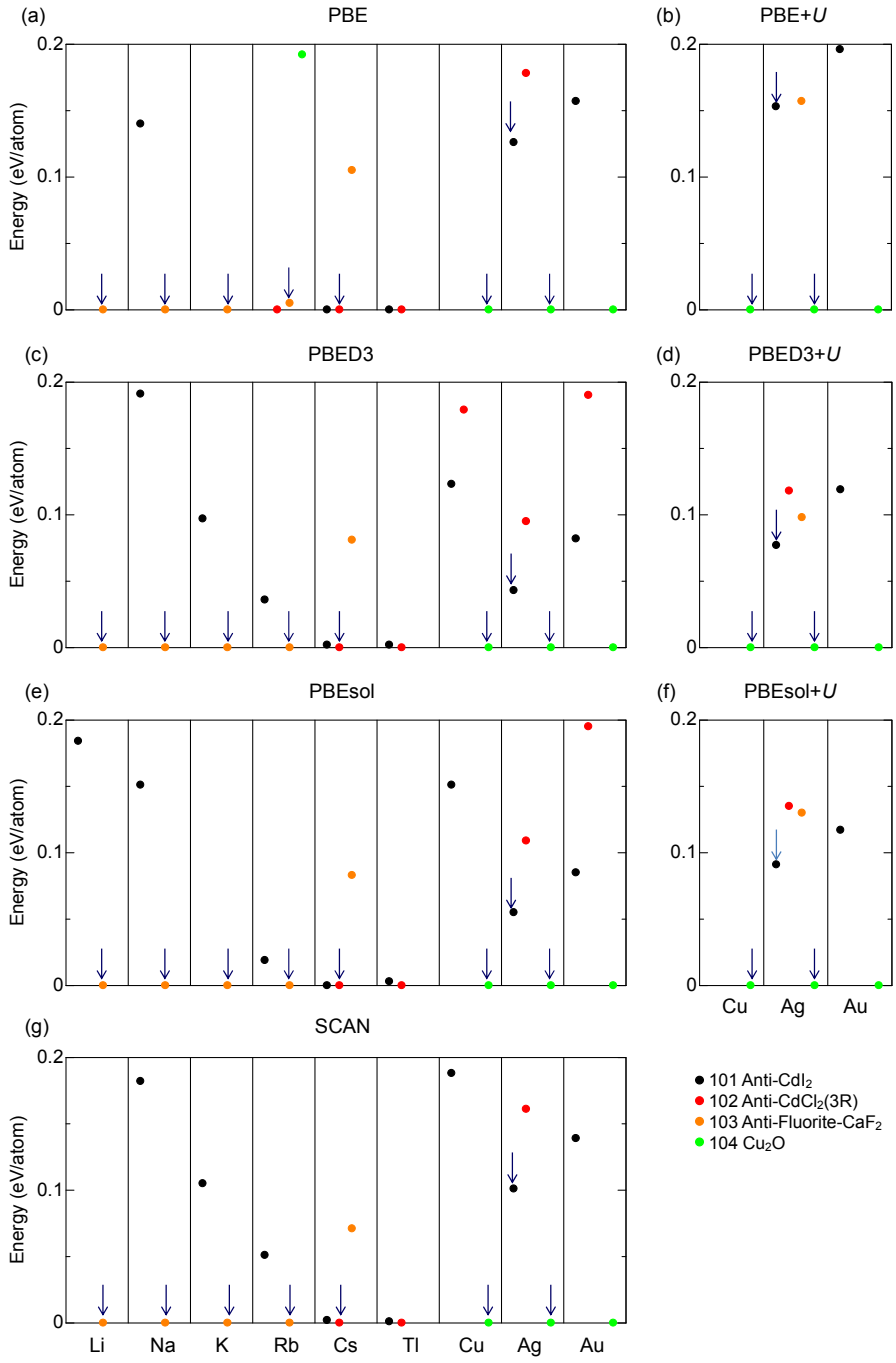

Fig. 6. Relative formation energies for monovalent cation oxides. Blue arrows indicate structures reported in the ICSD.

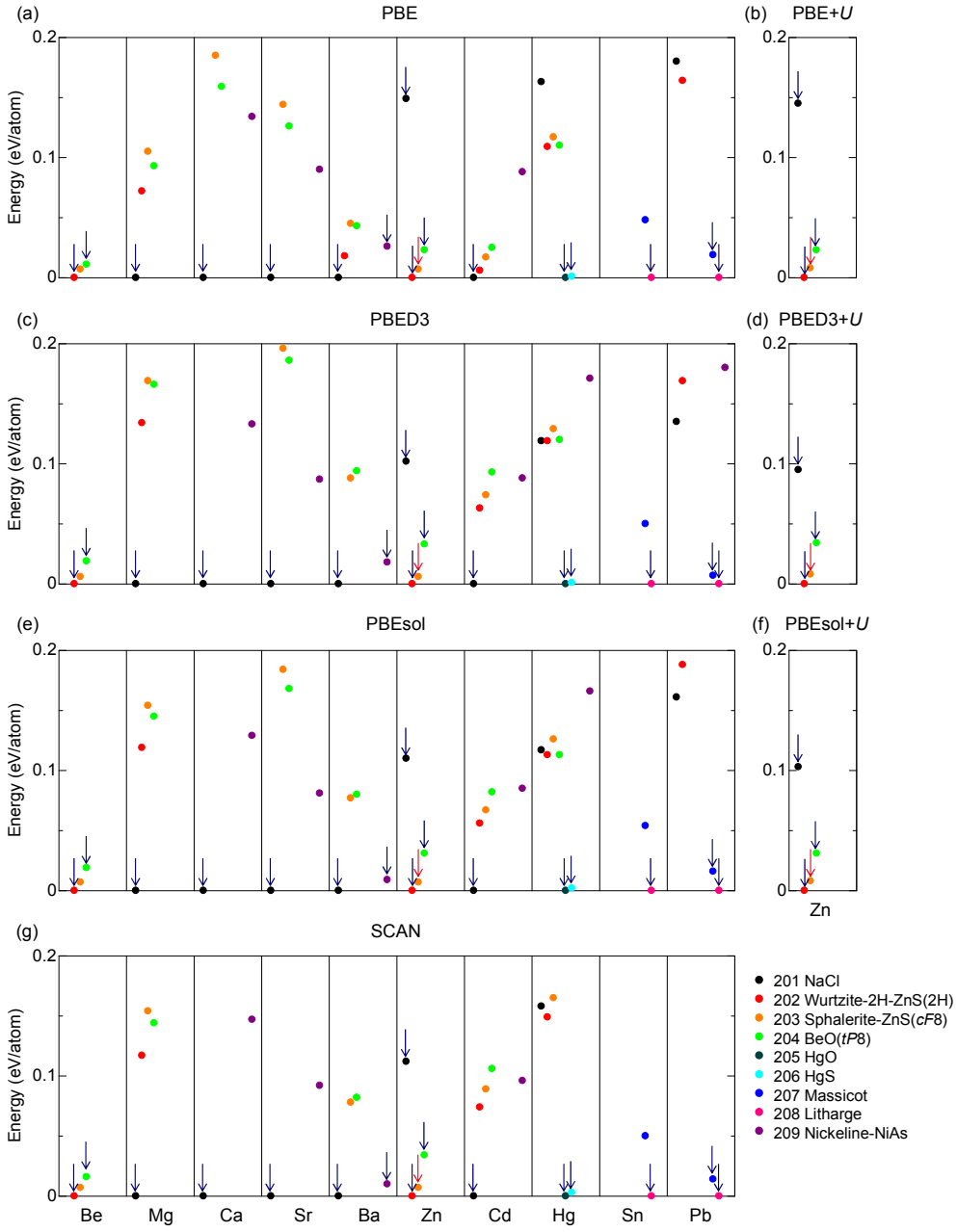

.

Fig. 7. Relative formation energies for divalent cation oxides. Blue arrows indicate structures reported in the ICSD, and red arrows are from another literature: ZnO in the 202 Sphalerite-ZnS (*cF*8) prototype [169].

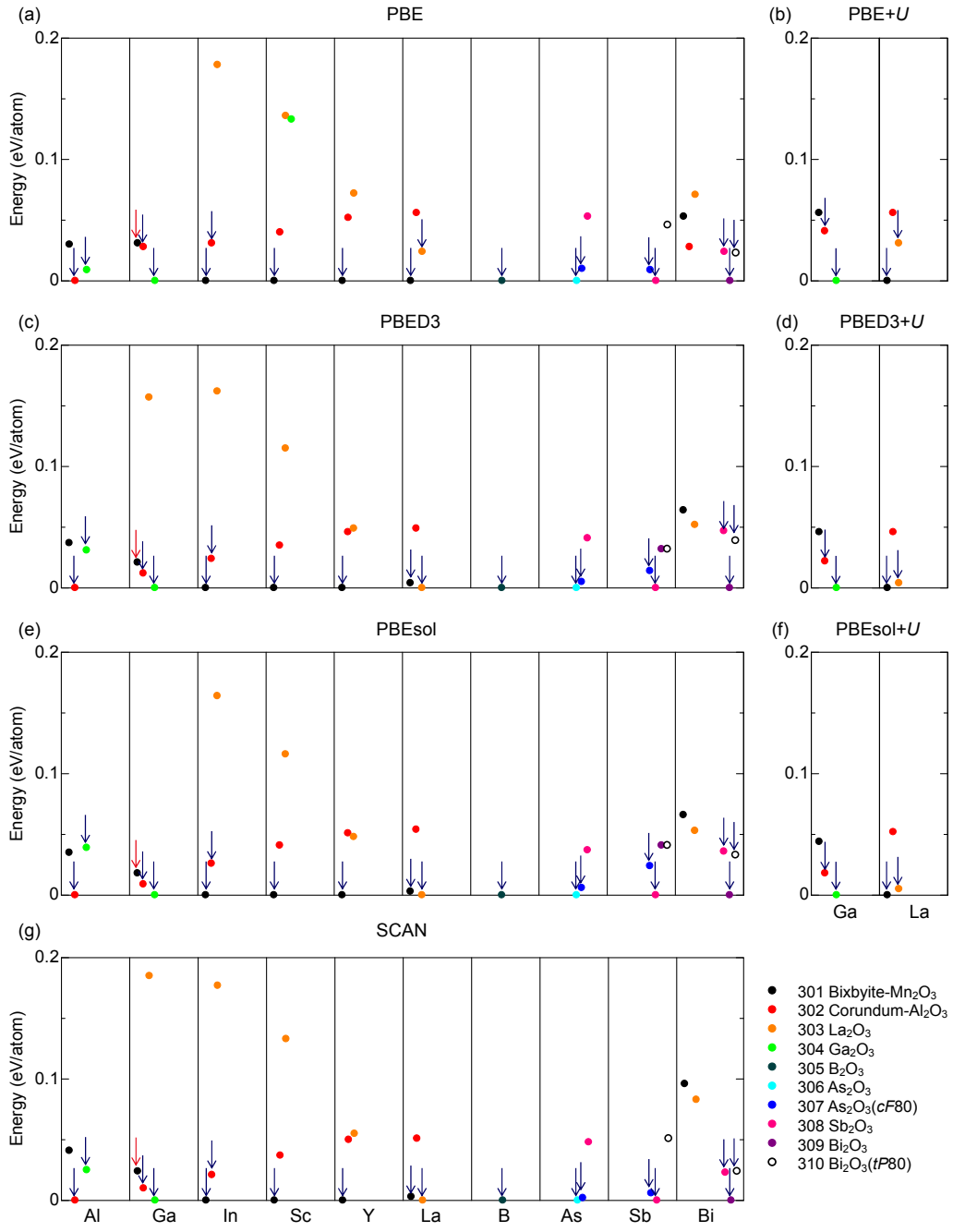

Fig. 8. Relative formation energies for trivalent cation oxides. Arrows indicate structures reported in the ICSD. Blue arrows indicate structures reported in the ICSD, and red arrows are from another literature: Ga_2O_3 in the 301 Bixbyite-Mn_2O_3 prototype [103].

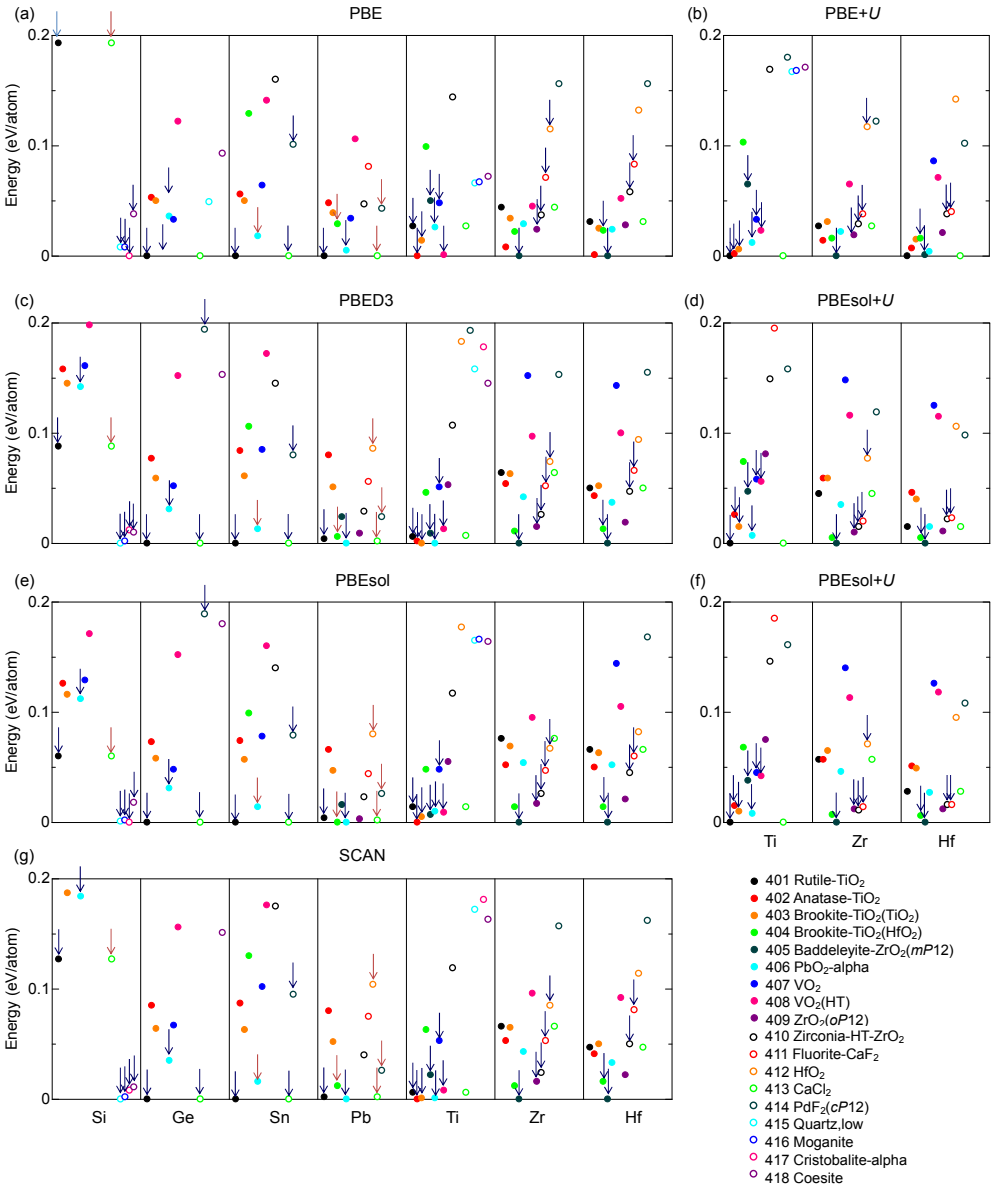

Fig. 9. Relative formation energies for quadrivalent cation oxides. Blue arrows indicate structures reported in the ICSD, and red arrows are from other literature: SiO_2 in the 413 $CaCl_2$ prototype [115], SnO_2 in the 406 PbO_2-alpha prototype [123,124], and PbO_2 in the 404 Brookite-TiO_2 (HfO_2), 412 HfO_2, 413 $CaCl_2$, and 414 PdF_2 (*cP*12) prototypes [126].

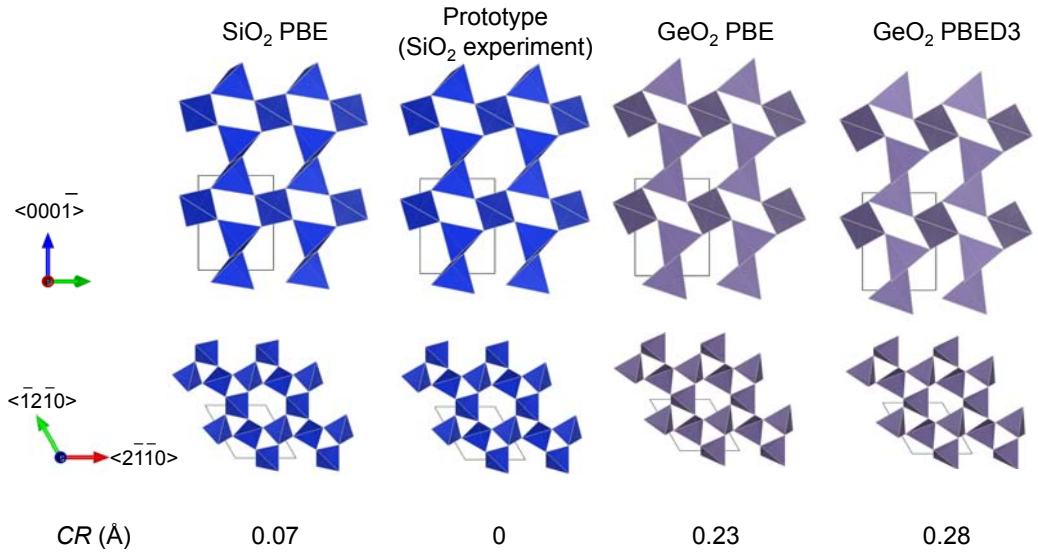

Fig. 10. Orientation of SiO_4 and GeO_4 tetrahedrons in the 415 Quartz-low structure as viewed from two different directions.

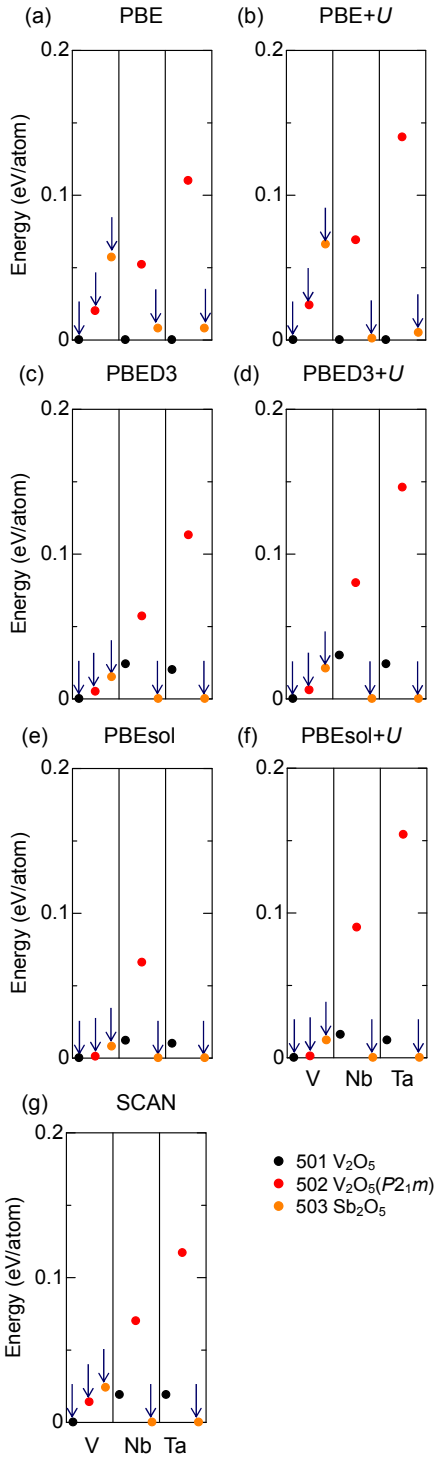

Fig. 11. Relative formation energies for pentavalent cation oxides. Blue arrows indicate structures reported in the ICSD.

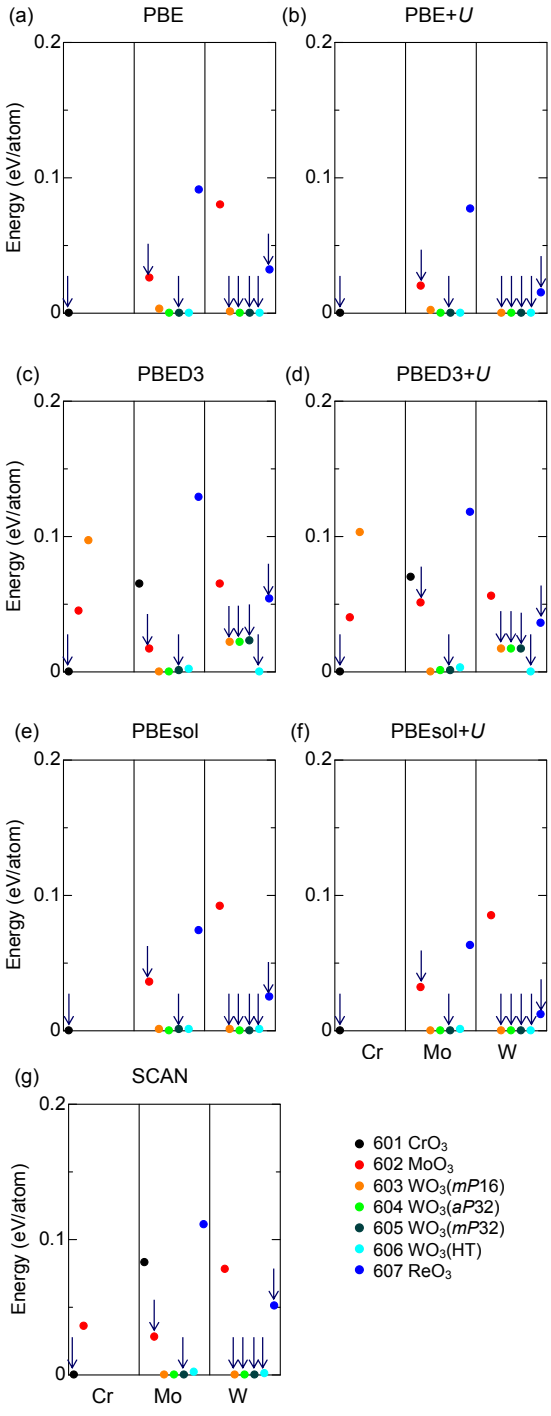

Fig. 12. Relative formation energies for hexavalent cation oxides. Blue arrows indicate structures reported in the ICSD.